

Chapter 2

Extrasolar Planetary Transits

Andrew Collier Cameron

Abstract An extrasolar planet will transit the visible hemisphere of its host star if its orbital plane lies sufficiently close to the observer's line of sight. The resulting periodic dips in stellar flux reveal key system parameters, including the density of the host star and, if radial-velocity observations are available, the surface gravitational acceleration of the planet. In this chapter I present the essential methodology for modelling the time-dependent flux variation during a transit, and its use in determining the posterior probability distribution for the physical parameters of the system. Large-scale searches for transiting systems are an efficient way of discovering planets whose bulk densities, and hence compositions, can be accessed if their masses can also be determined. I present algorithms for detrending large ensembles of light curves, for searching for transit-like signals among them. I also discuss methods for identifying diluted stellar eclipsing binaries mimicking planetary transit signals, and validation of transit candidates too faint for radial-velocity follow-up. I review the use of time-resolved spectrophotometry and high-resolution spectroscopy during transits to identify the molecular constituents of exoplanetary atmospheres.

2.1 Introduction to Exoplanetary Transits

If the orbital planes of extrasolar planetary systems are randomly oriented in space, a subset of them must lie in planes close enough to the line of sight that one or more planets in a system will transit the disk of the host star. Struve (1952) proposed the idea that the resulting periodic, temporary drops in stellar flux could be used as a planet detection method. Although Struve's idea pre-dated the technology needed to detect transits by half a century, his estimates of the likelihood of transits occurring, and of their depth and duration, have been borne out by observation over the last 15 years. Large-scale surveys from the ground have revealed that roughly one main-sequence star in 1000 hosts a gas-giant planet in the kind of orbit that Struve

A.C. Cameron (✉)

SUPA, School of Physics and Astronomy, University of St Andrews, North Haugh, St Andrews, KY16 9SS, UK

e-mail: acc4@st-andrews.ac.uk

envisaged. NASA's *Kepler* mission (Borucki et al. 2010) has extended the detection domain into the realm of planets down to terrestrial size, providing the first insights into the size and occurrence distributions of rocky, icy and gaseous planets.

In the first of this series of lectures I discuss the transit probability and its dependence on system geometry, then discuss the physical information that can be deduced in a model-independent way from transits.

2.1.1 Transit Probability

In the absence of any prior knowledge of the system's inclination, the probability of transits being visible over interstellar distances is given by the fraction of the celestial sphere swept out by the planet's shadow (Fig. 2.1).

From the observer's point of view, the apparent separation of the planet and star at mid-transit is conveniently expressed as a dimensionless impact parameter b , expressed in units of the host star's radius R_* :

$$b = \frac{a \cos i}{R_*}. \quad (2.1)$$

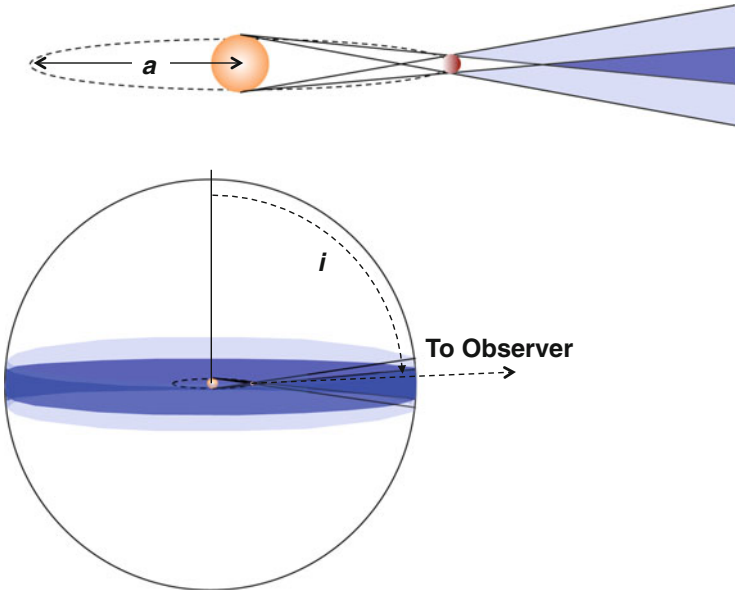


Fig. 2.1 Schematic view of the regions of the celestial sphere from which full (*dark shadow*) and grazing (*light shadow*) transits are visible

Here a is the semi-major axis of the orbit (assumed for the moment to be circular), and i is the angle between the angular-momentum vector of the planet's orbit and the line of sight. A grazing transit of a planet with radius R_p will have $R_* + R_p > a \cos i > R_* - R_p$. For a full transit to occur, the inequality $a \cos i > R_* - R_p$ must be satisfied.

The fraction of the solid angle on the celestial sphere enclosing cones with opening angles in the range i to $i + di$ is given by

$$\frac{d\Omega}{4\pi} = \frac{2\pi \sin i \, di}{4\pi} = \frac{d(\cos i)}{2}. \quad (2.2)$$

For randomly oriented orbits, the probability that grazing or full transits will occur is

$$\Pr\left(\cos i < \frac{R_* + R_p}{a}\right) = \frac{1}{2} \int_{-(R_* + R_p)/a}^{(R_* + R_p)/a} = \frac{R_* + R_p}{a}. \quad (2.3)$$

In the typical case where $R_p \ll R_*$, the probability of transits occurring is simply R_*/a .

$$\Pr\left(\cos i < \frac{R_*}{a}\right) \simeq 0.0046 \left(\frac{R_*}{R_\odot}\right) \left(\frac{1\text{au}}{a}\right). \quad (2.4)$$

This clearly favours the discovery of hot planets in close orbits around their host stars. Transits of Earth are visible from only 0.46 % of the celestial sphere. For Jupiter, orbiting 5.2 AU from the Sun, the probability is only 0.09 %. For this reason, transit surveys conducted with the goal of discovering planets at distances of order 1 AU from their host stars must monitor many thousands of objects for several years.

2.1.2 Early Detections

The first successful detections of extrasolar planets orbiting main-sequence stars were made via the radial-velocity method, which favours discovery of massive planets in close orbits around their host stars. The early radial-velocity discoveries such as 51 Peg b (Mayor and Queloz 1995) had minimum masses characteristic of gas-giant planets. Their radii were expected to be comparable to that of Jupiter, implying transit depths of order 1 %. The hot Jupiters typically lay about ten stellar radii from their host stars, giving roughly a one-in-ten chance that transits would be observable. Once orbital solutions were published, intensive high-precision photometric follow-up campaigns were conducted around the time of inferior conjunction.

Indeed HD 209458b, the 14th radial-velocity planet discovery to be published (Charbonneau et al. 2000; Henry et al. 2000), was the first system in which transits

were found to occur. The first detections were made on the nights of 1999 September 9 and 16 with the prototype STARE instrument, a small $f/2.9$ Schmidt camera of focal length 289 mm, operated on a tripod in the parking lot of the High-Altitude Observatory in Boulder, Colorado by then-graduate student David Charbonneau. Analysis of the transits yielded a fractional flux deficit $\Delta f/f = 1.7\%$ and duration from first to fourth contact of about 3 h.

2.1.3 Transit Depths and Durations

The fractional flux deficit at mid-transit corresponds approximately to the ratio of the projected areas of the planet and star (Fig. 2.2):

$$\frac{\Delta f}{f} \simeq \left(\frac{R_p}{R_*} \right)^2 = 0.0105 \left(\frac{R_p}{R_{\text{Jup}}} \right)^2 \left(\frac{R_*}{R_{\odot}} \right)^{-2}. \quad (2.5)$$

In practice, the transit depth overestimates the ratio of areas if the limb darkening of the stellar photosphere is not taken into account. For a star with specific intensity I_0 at disk centre and a linear limb-darkening law with limb-darkening coefficient u , the specific intensity of the point behind the centre of the planet at mid-transit is

$$I = I_0(1 - u(1 - \mu)) \quad (2.6)$$

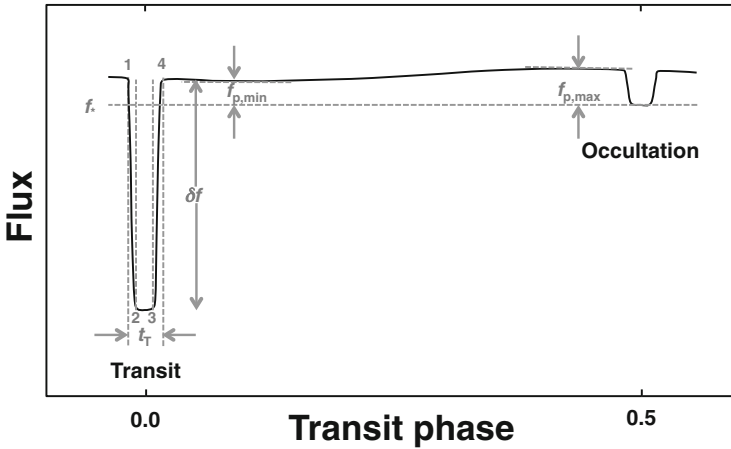
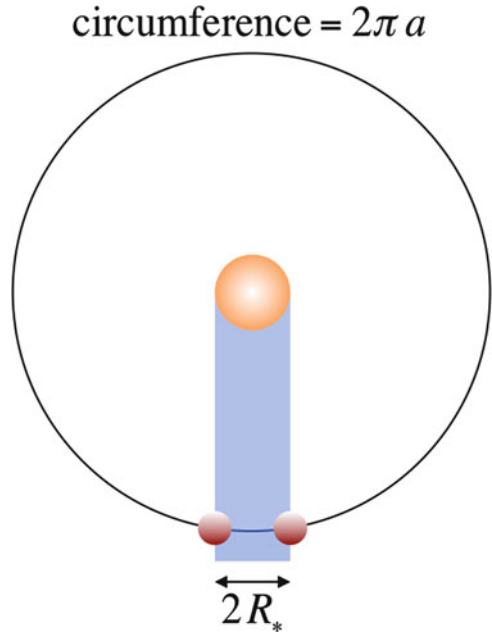


Fig. 2.2 Anatomy of the thermal-infrared light curve of a planet in a circular orbit. The first, second, third and fourth contact points of the transit are labelled; the total transit duration t_T is the duration from first to fourth contact. Outside transit and secondary occultation, the flux from the planet varies quasi-sinusoidally between $f_{p,\text{max}}$ when the hottest part of the dayside hemisphere faces the observer, and $f_{p,\text{min}}$ for the coolest part of the nightside. The flux level f_* of the star alone is seen only during occultation, when the planet is behind the star

Fig. 2.3 Schematic showing that the ratio of transit duration to orbital period is proportional to the ratio of the stellar radius to the orbital separation. The planet is shown at the mid-ingress and mid-egress positions where its centre lies on the stellar limb, as seen by an observer in the orbital plane



where the direction cosine $\mu = \cos \theta$ between the line of sight and the stellar surface normal at the planet's position is related to the impact parameter b by $\cos \theta = \sqrt{1 - b^2}$. If $R_p \ll R_*$ and the planet is completely dark, the ratio of the flux blocked by the planet to the total flux from the visible stellar hemisphere is

$$\begin{aligned} \frac{\Delta f}{f} &= \frac{\pi R_p^2 I_0 (1 - u + u \cos \theta)}{2\pi R_*^2 I_0 \int_0^{\pi/2} (1 - u + u \cos \theta) \sin \theta \cos \theta d\theta} \\ &= \frac{3(1 - u + u\sqrt{1 - b^2})}{3 - u} \left(\frac{R_p}{R_*} \right)^2. \end{aligned} \quad (2.7)$$

More realistic limb-darkening laws are discussed in Sect. 2.4.

For the simplified case of a planet in a circular orbit with inclination $i = 90^\circ$, the transit duration T from mid-ingress to mid-egress is related to the orbital period P by simple geometry:

$$\frac{T}{P} = \frac{1}{\pi} \sin^{-1} \frac{R_*}{a} \quad (2.8)$$

where a is the orbital semi-major axis. Using Kepler's third law to substitute for a (Fig. 2.3),

$$\frac{T}{P} = \frac{1}{\pi} \sin^{-1} R_* \left(\frac{4\pi^2}{GM_* P^2} \right)^{1/3}. \quad (2.9)$$

In the more general case where the inclination is less than 90° , the transit duration is reduced. Seager and Mallén-Ornelas (2003) generalise the time t_T from first to last contact as a function of inclination:

$$\frac{t_T}{P} = \frac{1}{\pi} \sin^{-1} \left(\frac{R_*}{a} \left\{ \frac{[1 + (R_p/R_*)]^2 - [(a/R_*) \cos i]^2}{1 - \cos^2 i} \right\}^{1/2} \right). \quad (2.10)$$

For $\cos i \ll 1$, and noting that $b = (a/R_*) \cos i$ for a circular orbit, this becomes

$$\frac{t_T}{P} = \frac{R_*}{\pi a} \sqrt{\left(1 + \frac{R_p}{R_*}\right)^2 - b^2}. \quad (2.11)$$

2.1.4 Model-Independent System Parameters

For the case where $R_* \ll a$, this leads to a model-independent relationship between the transit duration, the orbital period and the stellar bulk density ρ_* ,

$$T \simeq 3h \left(\frac{P}{4d} \right)^{1/3} \left(\frac{\rho_*}{\rho_\odot} \right)^{-1/3}. \quad (2.12)$$

If an orbital radial-velocity solution is available, it is also possible to measure the planetary surface gravity g_p using the radial acceleration of the star at conjunction and the transit duration. Again assuming a circular orbit with $i = 90^\circ$, the stellar orbital acceleration at conjunction is

$$\frac{dv_r}{dt} = \frac{2\pi K}{P} = \frac{GM_p}{a^2} = g_p \frac{R_p^2}{a^2} = g_p \frac{R_p^2}{R_*^2} \frac{R_*^2}{a^2}, \quad (2.13)$$

where K is the amplitude of the star's orbital reflex motion about its centre of gravity with the planet. Southworth et al. (2007) pointed out that since $(R_p/R_*)^2$ is related to the transit depth by Eq. (2.7) and (R_*/a) is related to the transit duration by Eq. (2.8), this provides a model-independent measure of the planet's surface gravitational acceleration,

$$g_p = \frac{2\pi K}{P} \left(\frac{R_*}{R_p} \right)^2 \left(\frac{a}{R_*} \right)^2. \quad (2.14)$$

To determine the planetary bulk density ρ_p requires a precise estimate of the stellar radius, as well as knowledge of the transit depth:

$$\rho_p = \frac{3g_p}{4\pi GR_p} = \frac{3g_p}{4\pi GR_*} \left(\frac{R_*}{R_p} \right). \quad (2.15)$$

If precise measures of the host star's angular diameter θ and parallax $\hat{\pi}$ (or distance d) are available, the planetary bulk density can also be derived independently of stellar models, since $R_* = \theta d = \theta / \hat{\pi}$:

$$\rho_p = \frac{3g_p\hat{\pi}}{4\pi G\theta} \left(\frac{R_*}{R_p} \right). \quad (2.16)$$

2.2 Transit Surveys

By the start of the twenty-first century, radial-velocity surveys of F, G, K and M stars had established that the occurrence rate of gas-giant planets orbiting within 0.1 AU of their host stars was about 1 % (Marcy et al. 2005). Such planets orbit close enough to their host stars to have transit probabilities of order 2–10 %. The transits of such planets have durations of order 3 h, short enough for complete events to be detected in the course of a single night from the ground. Detection of more distant planets is more difficult. At 1 AU from a star of 1 solar mass, the transit duration is 13 h and the probability of transits occurring is greatly reduced.

Despite being intrinsically rare, large close-orbiting planets have a sufficiently high transit probability that roughly one star in every thousand should host a transiting hot Jupiter. To achieve a yield of order 1000 hot Jupiters at a detection efficiency of 100 % requires at least one million stars to be monitored with a photometric precision better than 1 %.

2.2.1 Ground-Based Surveys

Transit searches became a high-priority goal for the optical gravitational lensing experiment survey (OGLE, Udalski et al. 1992), which was already monitoring millions of stars in the galactic bulge region using the 1.3-m Warsaw telescope at Las Campanas, Chile. Many dozens of transit candidates with V magnitudes between 15 and 16 were published by Udalski et al. (2002a,b,c), but efforts to establish their planetary nature via radial-velocity follow-up proved challenging even with the UVES instrument on the VLT (e.g. Bouchy et al. 2004, 2005) owing to the faintness of the host stars. A shallower, wider-field approach was needed to produce brighter candidates for which radial-velocity follow-up could be conducted efficiently on smaller telescopes.

The brightest known stars hosting transiting hot Jupiters are HD 209458 (magnitude $V = 7.6$) and HD 189733 ($V = 7.7$). Using the fact that a 5-magnitude increase in limiting magnitude accesses a volume of space 1000 times greater, and assuming these to be both representative and the only examples of their kind brighter than $V = 8.0$, simple extrapolation suggests that there ought to be at least 2000 similar objects brighter than $V = 13.0$. This is encouraging, because 1.2 m-class telescopes

with high-precision radial-velocity spectrometers such as CORALIE on the 1.2-m Euler telescope at La Silla and SOPHIE in the 1.9-m telescope at Haute-Provence are capable of performing the essential radial-velocity follow-up at magnitudes brighter than $V = 12.0$ or so. The whole sky comprises 41,253 square degrees, so there should be at least one transiting hot Jupiter brighter than $V = 12.0$ per 82 square degrees of sky.

The image scale of a telescope of focal length f is

$$3600 \times \frac{180}{\pi} \frac{1}{f} = \frac{206265}{f} \text{ arcsec/mm}, \quad (2.17)$$

if f is expressed in mm. To image 82 square degrees of sky on to an affordable science-grade charge-coupled device (CCD) of 2048^2 $13.5 \mu\text{m}$ pixels requires a telescope with a focal length of 174 mm.

These considerations inspired several groups to embark on ground-based surveys employing commercial 200-mm camera lenses on robotic mounts backed by science-grade CCDs. The image scale of these 200-mm lenses is

$$3600 \times \frac{180}{\pi} \frac{1}{f} = 1031 \text{ arcsec/mm}, \quad (2.18)$$

yielding a pixel scale

$$0.0135 \times 1031 = 13.9 \text{ arcsec/pixel} \quad (2.19)$$

and hence a field of view whose angular extent is

$$\frac{2048 \times 13.9}{3600} = 7.9 \text{ degrees}, \quad (2.20)$$

with a solid angle of 62 square degrees. The expected planet catch is therefore of order one hot Jupiter brighter than $V = 12.0$ per camera. The most successful among these surveys have been the transatlantic exoplanet survey (TrES, Alonso et al. 2004); the wide-angle search for planets (WASP, Pollacco et al. 2006), the Hungarian automated telescope network (HATNet, Bakos et al. 2004) and the XO survey (McCullough et al. 2005). More recently, HATSouth (Bakos et al. 2013), the Qatar exoplanet survey (QES, Alsubai et al. 2013) and the kilodegree extremely little telescope (KELT, Pepper et al. 2007) have entered service and started publishing new discoveries of transiting planets. Together they have surveyed about 80 % of the sky (Fig. 2.4), and published over 180 confirmed discoveries of transiting gas-giant and ice-giant planets brighter than $V = 13.0$ with periods less than 10 days. The mass–radius diagram for these ground-based discoveries is shown in Fig. 2.5.

The next-generation transit survey (NGTS, Wheatley et al. 2014) builds on the experience of the WASP survey, with the goal of detecting transits 0.001 magnitude

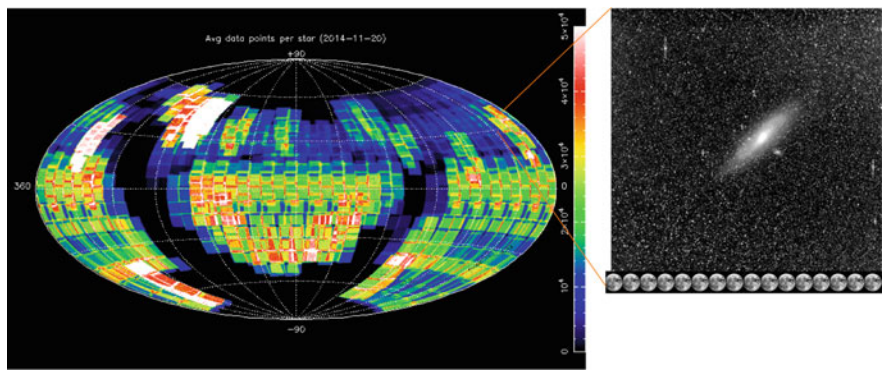


Fig. 2.4 Sky coverage of the WASP survey. The *colour scale* denotes the number of exposures in the archive for a given field, from *black* (0) to *white* (50,000 images). The average field has been observed 25,000 times over 2 or 3 seasons. The 8-camera “footprint” of the instrument is apparent. The zoomed image at right illustrates the 7.8-degree square field of view of a single camera

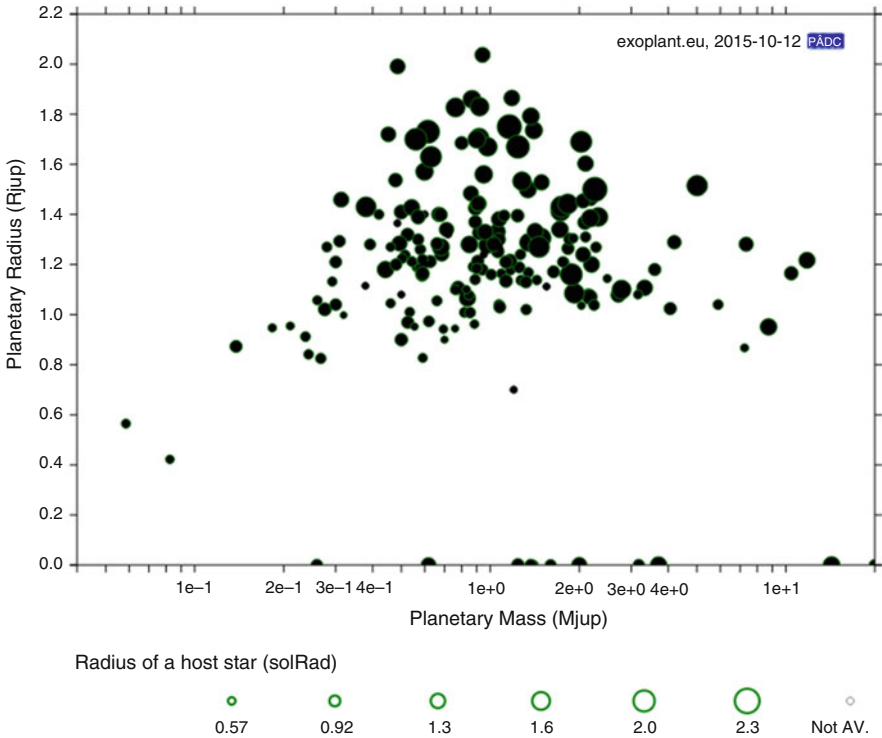


Fig. 2.5 Planetary mass–radius diagram for ground-based discoveries from the TrES, WASP, HATNet, XO, HATSouth, QES and KELT surveys. *Symbol size* denotes host star radius, illustrating that inflated planets tend to orbit large stars, and that small planets are more easily detected around smaller host stars

deep from the ground. It comprises 12 small robotic telescopes located at Paranal, Chile. As discussed in Sect. 2.3.4, colour-dependent flat-fielding errors dominate the WASP error budget at bright magnitudes. Experiments with the prototype NGTS instrument have verified that the required noise levels can be achieved with sub-pixel guiding precision. The 600–900 nm passband of NGTS is designed to probe the short-period population of large super-Earths and mini-Neptunes orbiting K and early M dwarfs. The resulting discoveries will be significantly brighter than their *Kepler* counterparts, making them viable targets for radial-velocity mass determination, and ultimately for transmission and occultation spectroscopy studies with the *James Webb Space Telescope* (JWST, Gardner et al. 2006).

2.2.2 Space-Based Surveys

Ground-based surveys are limited in their ability to detect small planets and planets in long-period orbits. Atmospheric transparency fluctuations and scintillation limit the relative photometric precision attainable from the ground to 0.1 % or so from the very best sites, while the Earth’s rotation precludes reliable detection of transits of more than 5 or 6 h duration.

Earth-sized planets have radii that are an order of magnitude smaller than Jupiters, with transit depths of order:

$$\left(\frac{R_{\oplus}}{R_{\odot}}\right)^2 \simeq 10^{-5}. \quad (2.21)$$

Space-based CCD photometry with sub-pixel pointing precision can attain a relative precision of order 10^{-5} with rigorous ensemble photometry and decorrelation (see Sect. 2.3). The long stare times needed to detect planets in long-period orbits can be achieved either by placing the spacecraft in independent orbit around the Sun or (more cheaply) in a near-polar Sun-synchronous low-Earth orbit, pointing away from the Sun.

The *CoRoT* mission, which remained operational for 6 years from launch in December 2006–November 2012, comprised a 27-cm telescope with a field of view of 2.7×3.05 degrees in a 900-km polar orbit (Auvergne et al. 2009). The orbit plane drifted only very slowly in right ascension, allowing a series of 5-month campaigns to be conducted in fields located close to the two intersections of the galactic plane with the ecliptic. Among the 28 planets published to date from the *CoRoT* mission, CoRoT-7b (Queloz et al. 2009) is distinguished as being the first example of a “super-Earth”, with a radius of $1.7 R_{\oplus}$ and an Earth-like density suggesting a predominantly iron-silicate composition (Haywood et al. 2014).

NASA’s *Kepler* mission (Borucki et al. 2010) is a Schmidt telescope with an effective aperture of 0.95 m, whose focal plane is tiled with 42 CCDs giving a field of view of 115 square degrees at an image scale of 4 arcsec per pixel. *Kepler*

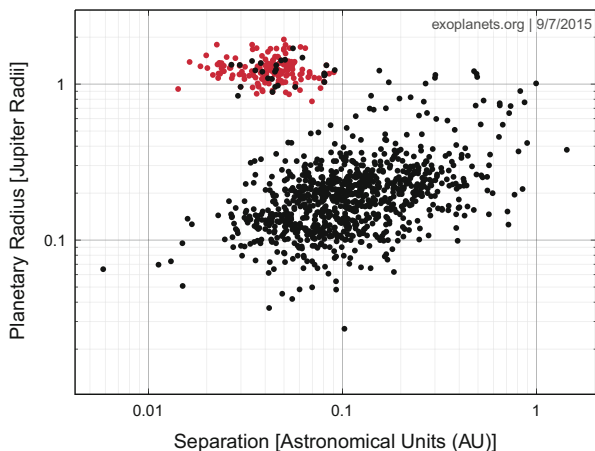


Fig. 2.6 Planetary radius-separation diagram for hot Jupiters found in ground-based surveys (*red*) and planet candidates with measured radii from the *Kepler* archive (*black*). In both cases, the *lower right-hand* boundary represents the transit-detection threshold. Hot Jupiters are intrinsically rare, even though they dominate ground-based surveys

was launched in 2009 May into an Earth-trailing heliocentric orbit. The baseline mission was to observe a single field, roughly midway between the bright stars Deneb and Vega, for 3.5 years. The focal plane detector configuration has fourfold symmetry, to allow for a 90° rotation around the boresight every 3 months, to maintain illumination of the solar panels.

Figure 2.6 shows clearly that the transit candidates with measured radii in the archive from *Kepler's* baseline mission occupy a very different part of mass-separation space to that occupied by the hot Jupiters from the ground-based surveys. Hot Jupiters are easily detected, so the *Kepler* points give a clearer impression of their paucity in comparison to the ice-giant and super-Earth planets that dominate the *Kepler* population.

Shortly after the baseline mission was extended in 2013, the *Kepler* spacecraft suffered a failure of its third remaining gyroscope. A new mode of operation, the K2 mission, is currently in progress (Howell et al. 2014). In this mode, *Kepler* points to targets near the ecliptic plane, slowing the rate of drift caused by unbalanced radiation pressure on its solar panels. A different field is selected each quarter. Although the pointing is less stable, careful decorrelation restores photometric precision roughly a factor 2 poorer than was achieved in the original mission. In addition to transit hunting, K2 permits a wider range of astrophysical investigations to be conducted than was possible with the original mission.

2.3 Ensemble Photometry and Transit Detection

Wide-field imaging photometry at optical wavelengths is performed using CCD detectors. In this section, I describe the key steps in the data processing for a ground-based wide-field photometry survey. The procedures described here follow closely those used in the WASP project, as described by Collier Cameron et al. (2006). The instrumentation, observing principles and data-reduction strategies of the HAT and WASP projects are described by Bakos et al. (2004, 2013) and Pollacco et al. (2006), respectively.

2.3.1 Image Preprocessing

Successful detection of transits with depths of 1 % or less requires meticulous care at every stage in the image processing (Fig. 2.7). At the start of each night, the cameras record sequences of zero-exposure frames, to map any spatial variation in the bias signal applied to the amplifier while the image is being read out. Dark frames, taken with the shutter closed and exposure times equal to the science frames, map the thermal noise pattern of the CCD. Once bias-subtracted, they may be subtracted from the science frames.

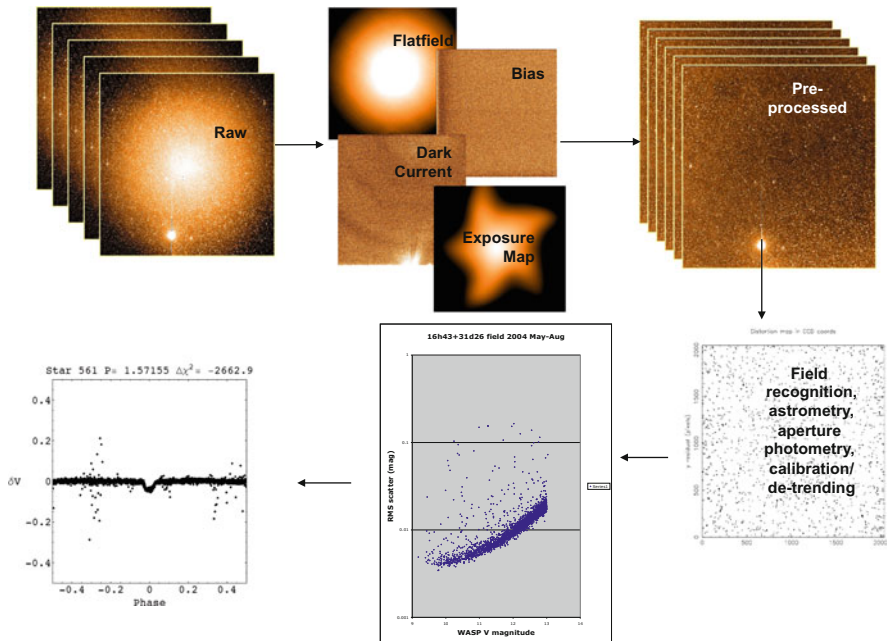


Fig. 2.7 Flow diagram illustrating the main steps in the WASP data-reduction pipeline

The relative sensitivities of individual pixels in the image are mapped using a sequence of “flat-field” exposures of the sky near the zenith, taken in dusk and dawn twilight. Exposure times are adjusted for each exposure according to a model of the sky brightness as a function of solar zenith angle at mid-exposure. Between exposures, the camera mount is moved slightly, to ensure that stellar images do not fall on the same pixels.

The resulting stack of images contains information about the brightness gradient of the twilight sky, the vignetting pattern of the optical system and the variation in exposure over the frame resulting from the finite travel time of the mechanical CCD shutter. The shutter travel time is measured from the linear dependence of the signal (relative to the image median) in a given pixel, as a function of inverse exposure time. The signal in each pixel is then scaled to give a uniform exposure time across the image, for both flat field and science frames. The large-scale variations in the individual flat fields are decomposed into a linear sky illumination gradient and a centro-symmetric vignetting pattern. The gradient is removed and the flat fields are normalised to their median signal values. Finally, the median of the individual flat-field images is computed, to eliminate any stellar images.

In practice, clouds or technical problems prevent acquisition of the flat-field sequences on some nights. Flat fields evolve with time. In the WASP and HAT cameras, for example, dust particles on the optical surfaces come and go, producing shadow discs with finite lifetimes. WASP employed a weighted average of historical flat-field images, using a weighting function which decayed exponentially with a time constant of 2 weeks.

The WASP data-reduction pipeline employs catalogue-driven aperture photometry. For each frame, an automated object-detection routine determines the positions of all point sources on the frame. The catalogue of object positions is cross-matched against the TYCHO-2 catalogue (Høg et al. 2000), and establishes an astrometric frame solution with an RMS precision of 0.1–0.2 pixel. The pipeline carries out aperture photometry at the positions of all objects brighter than magnitude 15.0 in the red bandpass of the USNO-B1.0 catalogue. The aperture photometry is carried out in three concentric circular apertures with radii of 2.5, 3.5 and 4.5 pixels. The flux ratios between pairs of apertures contain information about image morphology. They are used to detect and flag blended pairs of images. The relationship between raw instrumental magnitude and TYCHO-2 V magnitude is established via a colour-dependent transformation. Further details of the image preprocessing are given in Sect. 4 of Pollacco et al. (2006).

2.3.2 Decorrelation

At this stage, the raw instrumental magnitudes are subject to various sources of systematic error. Foremost among these is atmospheric extinction. The attenuation of light from each object depends on the wavelength dependence of scatterers in the Earth’s atmosphere and the path length through the atmosphere. The airmass X is

the path length scaled to that at the zenith, and varies with zenith angle z as $\sec z$. The intensity along the incoming beam decays exponentially with X . The observed magnitude m_{obs} is related to the magnitude m_0 observed above the atmosphere by

$$m_{\text{obs}} = m_0 + kX. \quad (2.22)$$

The extinction coefficient k is itself dependent on the colour of the star. This arises because k increases with decreasing wavelength, due to Rayleigh and other scattering processes. If a wide bandpass is used, intrinsically red stars will suffer less extinction than bluer ones. Expressed in terms of a star's colour index c , the extinction equation becomes

$$m_{\text{obs}} = m_0 + k'X + k''cX, \quad (2.23)$$

where k' and k'' are referred to as the primary and secondary extinction coefficients.

Correcting for secondary extinction is problematic if, as is generally the case, the colour of the star is not known in advance. To make matters worse, the extinction coefficient varies slowly across the sky at many sites, and can change with time-dependent factors such as local wind speed, direction and humidity. To combat this, Tamuz et al. (2005) devised a generalised iterative scheme, known as SYSREM, for the correction of extinction and other systematics that vary smoothly across the field of view as a function of time.

SYSREM operates on a rectangular array of light curves of N objects, each of which is observed at M different epochs. Before applying the SYSREM algorithm, the WASP pipeline carries out a maximum-likelihood coarse decorrelation to determine the mean magnitude and variance of each of the N stars, and the zero-point correction and its variance for each of the M images. The mean magnitude of each star is

$$\hat{m}_i = \frac{\sum_j m_{i,j} w_{i,j}}{\sum_j w_{i,j}}, \quad (2.24)$$

where the weight $w_{i,j} = 1/(\sigma_{i,j}^2 + \sigma_{t(j)}^2)$ includes both the estimated variance of the observed magnitude and an additional intra-frame variance $\sigma_{t(j)}^2$ which serves to down-weight images degraded, for example, by drifting cloud.

Similarly, the zero-point correction for each frame is

$$\hat{z}_j = \frac{\sum_i m_{i,j} u_{i,j}}{\sum_i u_{i,j}}, \quad (2.25)$$

where the weight $u_{i,j} = 1/(\sigma_{i,j}^2 + \sigma_{s(i)}^2)$ includes both the estimated variance of the observed magnitude and an additional per-star variance $\sigma_{s(i)}^2$ which serves to down-weight stars with high intrinsic variability.

To solve for $\sigma_{s(i)}^2$, consider the likelihood of obtaining a data vector $\mathbf{D} = \{m_{i,j}, j = 1 \dots M\}$ for star i conditioned on a model $\boldsymbol{\mu} = \{\hat{m}_i + \hat{z}_j, j = 1 \dots M\}$ assuming Gaussian noise:

$$L(\mathbf{D}|\boldsymbol{\mu}) = (2\pi)^{-M/2} \prod_j \left[\frac{1}{\sigma_{i,j}^2 + \sigma_{t(j)}^2 + \sigma_{s(i)}^2} \right] \times \exp \left\{ -\frac{1}{2} \chi_i^2 \right\} \quad (2.26)$$

where

$$\chi_i^2 = \sum_j \frac{(m_{i,j} - \hat{m}_i - \hat{z}_j)^2}{\sigma_{i,j}^2 + \sigma_{t(j)}^2 + \sigma_{s(i)}^2}. \quad (2.27)$$

To obtain the maximum-likelihood solution, we first solve iteratively for $\sigma_{s(i)}^2$ holding $\sigma_{t(j)}^2$ constant:

$$\sum_j \frac{1}{\sigma_{i,j}^2 + \sigma_{t(j)}^2 + \sigma_{s(i)}^2} - \sum_j \frac{(m_{i,j} - \hat{m}_i - \hat{z}_j)^2}{\left[\sigma_{i,j}^2 + \sigma_{t(j)}^2 + \sigma_{s(i)}^2 \right]^2} = 0. \quad (2.28)$$

Analogously, we solve iteratively for $\sigma_{t(j)}^2$ holding $\sigma_{s(i)}^2$ constant:

$$\sum_i \frac{1}{\sigma_{i,j}^2 + \sigma_{t(j)}^2 + \sigma_{s(i)}^2} - \sum_i \frac{(m_{i,j} - \hat{m}_i - \hat{z}_j)^2}{\left[\sigma_{i,j}^2 + \sigma_{t(j)}^2 + \sigma_{s(i)}^2 \right]^2} = 0. \quad (2.29)$$

The entire system of equations (2.24), (2.25), (2.28) and (2.29) is then iterated to convergence to give \hat{m}_i , \hat{z}_j , $\sigma_{s(i)}^2$ and $\sigma_{t(j)}^2$.

We start by subtracting the inverse variance-weighted average magnitude of each star and the zero point of each frame to obtain a residual array

$$r_{i,j} = m_{i,j} - \hat{m}_i - \hat{z}_j. \quad (2.30)$$

SYREM is applied to this residual array. The goal is to minimise the misfit S^2 between the residuals and a model consisting of the product of the extinction coefficient c_i for each star and the airmass a_i at the time of observation. The misfit statistic for star i is

$$S_i^2 = \sum_j (r_{i,j} - a_i c_j)^2 w_{i,j}, \text{ where } w_{i,j} = \frac{1}{\sigma_{i,j}^2 + \sigma_{t(j)}^2 + \sigma_{s(i)}^2}. \quad (2.31)$$

Since the average airmass a_j of each frame is known, we can now determine an effective “extinction coefficient” for each star by optimal scaling:

$$c_i = \frac{\sum_j r_{i,j} a_j w_{i,j}}{\sum_j a_j^2 w_{i,j}}. \quad (2.32)$$

Similarly, the problem can be re-cast to determine the optimal effective airmass a_j for each image, given the effective extinction coefficients c_i for the individual stars:

$$a_j = \frac{\sum_i r_{i,j} c_i w_{i,j}}{\sum_i c_i^2 w_{i,j}}. \quad (2.33)$$

Once again, the system is iterated to convergence to obtain optimal sets of c_i and a_j . Tamuz et al. (2005) find that the algorithm converges to the same values irrespective of the values used for the initial airmasses. The final c_i and a_j are not therefore necessarily related to stellar extinction coefficients and airmasses. For example, steadily declining temperature during the night can induce a drift in focus which affects stars in different parts of the field to a greater or lesser extent. The same approach can be used to model further systematics with this kind of linear behaviour in the residuals from the initial calculation:

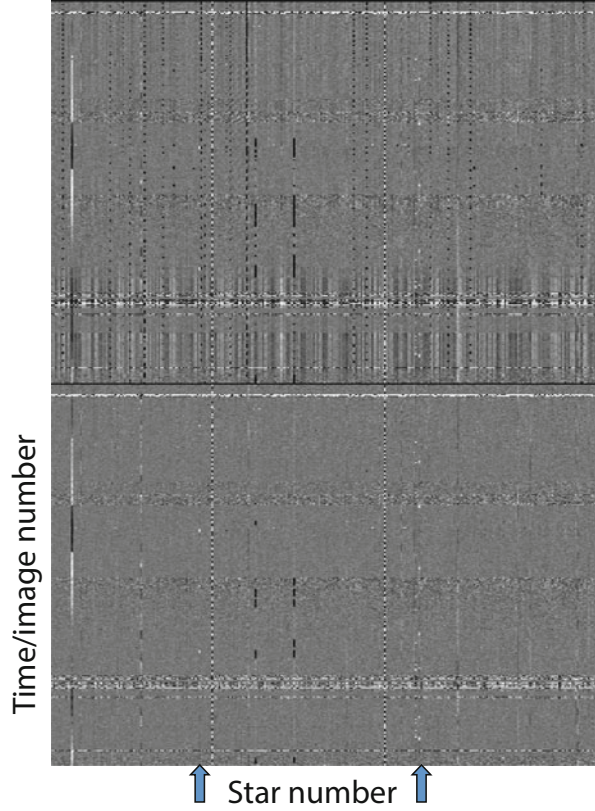
$$^{(1)}r_{i,j} = r_{i,j} - ^{(1)}c_i ^{(1)}a_j, \quad (2.34)$$

by minimising

$$^{(1)}S_i^2 = \sum_{i,j} (^{(1)}r_{i,j} - ^{(2)}c_i ^{(2)}a_j)^2 w_{i,j} \quad (2.35)$$

The procedure is very similar to principal-component analysis (PCA), and indeed reduces to PCA in the case where all the data weights are identical. The WASP pipeline computes and corrects for the four most significant sets of basis vectors $^{(k)}a_j$ and $^{(k)}c_i$. This is sufficient to remove the most significant sources of instrumental and environmental systematic error that are common to all stars in the field, while preserving genuine astrophysical variability (Fig. 2.8). Other decorrelation methods to which the reader is referred include the trend filtering analysis (TFA, Kovács et al. 2005), which is used in both HAT and WASP transit searches. External parameter decorrelation (EPD, Bakos et al. 2010) is a parametric decorrelation method using basis functions constructed from factors known or suspected to cause systematic error such as pixel coordinates and sub-pixel phase, sky background level, point-spread function shape parameters, hour angle and zenith distance. EPD and SYSREM are generally applied before TFA. A more rigorous Bayesian approach analogous to SYSREM and TFA (Smith et al. 2012) is used to generate the cotrending basis vectors for the maximum a posteriori pre-search conditioning (PDC-MAP) data products from the *Kepler* mission. More recently, Gibson (2014)

Fig. 2.8 Application of SYSREM to the ensemble of light curves from WASP field 16h30+28. The *upper panel* shows the residual array in *greyscale* form following subtraction of the mean magnitude of each star and the zero point of each frame. Each column is the light curve of one star; each row holds data from a single image. The *lower panel* shows the same data after removal of four SYSREM basis functions. The *arrows* denote two objects exhibiting occasional transit-like events



and Aigrain et al. (2015) have developed non-parametric equivalents of EPD employing Gaussian-process regression to model the systematics in HST/NICMOS, Spitzer and K2 photometry.

2.3.3 Transit Detection

The most widely used transit-detection method is the box least-squares (BLS) method of Kovács et al. (2002). Following decorrelation, we compute and subtract the optimal average magnitude of the observations \hat{x}_j of a given star as

$$x_j = \bar{x}_j - \frac{\sum_j \bar{x}_j w_j}{\sum_j w_j} \quad (2.36)$$

where w_j includes the stellar-variability and spatial-transparency variances as in Eq. (2.31).

We also define the global summations

$$t = \sum_j w_j \text{ and } \chi_0^2 = \sum_j x_j^2 w_j, \quad (2.37)$$

assuming the noise to be uncorrelated.

The transit search is conducted on a frequency grid. The frequency spacing must satisfy the requirement that the phase of each observation must change by less than the transit duration between adjacent frequencies. At each frequency the data are sorted in phase and partitioned into blocks of in-transit (ℓ , low) and out-of-transit (h , high) points. Different transit phases are explored by repartitioning with the low block at a succession of locations along the phase-sorted dataset, and summing within the low block:

$$s = \sum_{i \in \ell} x_i w_i, \quad r = \sum_{i \in \ell} w_i, \quad q = \sum_{i \in \ell} x_i^2 w_i. \quad (2.38)$$

The mean light level in transit (L) and its variance are given by

$$L = \frac{s}{r}, \quad \text{Var}(L) = \frac{1}{r}, \quad (2.39)$$

while outside transit

$$H = \frac{-s}{t-r}, \quad \text{Var}(H) = \frac{1}{t-r}. \quad (2.40)$$

The fitted transit depth and its associated variance are

$$\delta = L - H = \frac{st}{r(t-r)}, \quad \text{Var}(\delta) = \frac{t}{r(t-r)}, \quad (2.41)$$

yielding the signal-to-noise ratio of the transit depth

$$\text{S/N} = s \sqrt{\frac{t}{r(t-r)}}. \quad (2.42)$$

The improvement in the fit to the data when compared with that of a constant light-curve model is, assuming uncorrelated noise,

$$\Delta\chi^2 = \frac{s^2 t}{r(t-r)}. \quad (2.43)$$

The goodness of fit outside transit is then,

$$\chi_h^2 = \chi_0^2 - \frac{s^2}{(t-r)} - q. \quad (2.44)$$

At each frequency, the values of the transit depth, $\Delta\chi^2$ and χ_h^2 , are stored for the transit phase that yields the best fit.

When transits are clearly detected, the resulting periodogram of $\Delta\chi^2$ usually shows a clear minimum at the orbital period. Harmonics of the orbital period are usually present at multiples and submultiples of the true period. For observations made from a single site, their relative strengths depend on the window function arising from the visibility of transits during the day/night cycle (Fig. 2.9). In practice, however, simple algorithms such as BLS are susceptible to false alarms, and human inspection of the light curves phase-folded at the dominant frequency is essential to verify whether or not genuine transits are present.

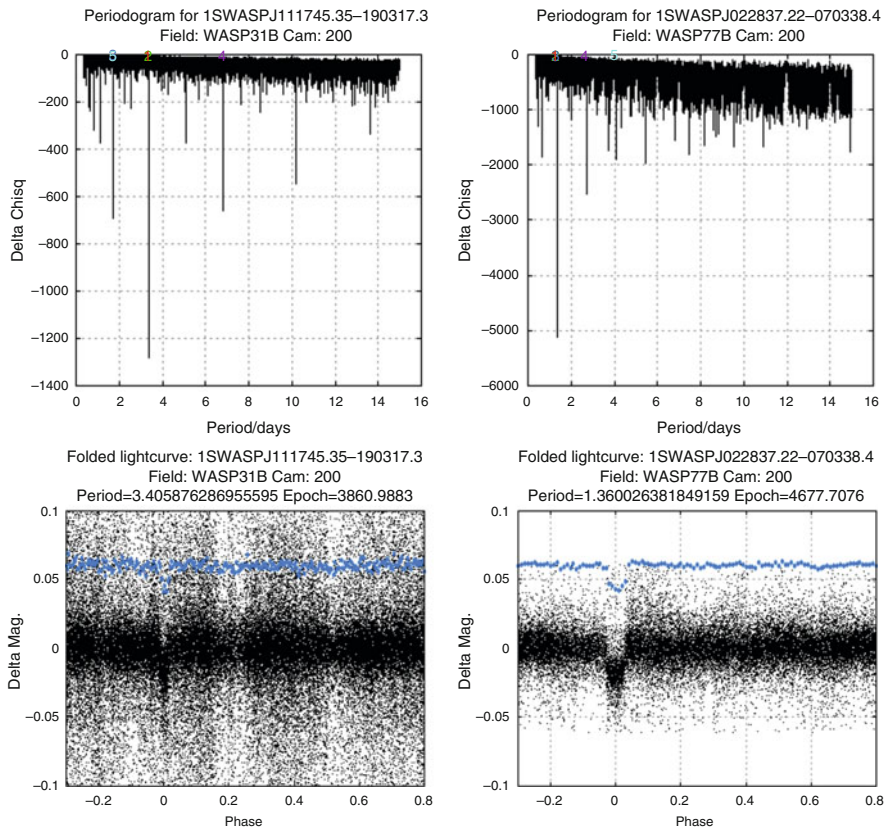


Fig. 2.9 BLS periodograms (*upper*) and folded transit light curves (*lower*) for two WASP planets: WASP-31b ($P = 3.40$ days, *left*) and WASP-77b ($P = 1.36$ days, *right*). Note spacing of harmonics at multiples of P and $P/2$, indicating that multiple transits are clearly detected

2.3.4 Correlated Noise

The treatment in Sect. 2.3.3 above yields the improvement in χ^2 relative to a constant-flux model with no transits. If the residual noise after decorrelation were Gaussian and independent, Bayesian model-comparison tools could be used to determine whether transits are present. In practice, however, correlated noise remains. At the instrumental level, imperfect flat fielding arising from transient dust particles on the optics and the colour dependence of the CCD pixel sensitivity pattern introduces complex position-dependent flux variations on a variety of length scales. At the astrophysical level, stellar p -modes, granulation and magnetic activity introduce correlated brightness fluctuations on a wide variety of timescales. A realistic assessment of the likelihood function ideally requires an understanding of the structure of the full covariance matrix.

Methods such as Gaussian-process regression provide powerful tools for modelling correlated noise sources in a non-parametric way. Unfortunately they are computationally inefficient for datasets of more than a few hundred data points. Pont et al. (2006) developed a simple approach for assessing the contributions of correlated noise on different timescales. The data are boxcar-smoothed on a succession of box lengths L . The empirical power-law dependence of the RMS scatter in the binned light curve on L takes the form of a power law:

$$\sigma_{\text{binned}} = \sigma_{\text{unbinned}} L^b. \quad (2.45)$$

If the noise is uncorrelated, we expect $b = -1/2$; completely correlated noise arising from variability on timescales intermediate between the longest smoothing length considered and the length of the data train gives $b = 0$.

Carter and Winn (2009) pointed out that when correlated noise is present whose power spectral density varies with frequency f as an inverse power law $1/f^\gamma$, the covariance matrix of the noise process is nearly diagonal when the data are transformed into a wavelet basis. For more or less evenly sampled data, this gives a fast and efficient method for calculating relative likelihoods and obtaining reliable estimates of parameter uncertainties.

2.4 Transit Parameter Fitting

As discussed in Sect. 2.1.3, the fraction of the host star's light blocked during a transit depends on the planet-to-star area ratio, the inclination of the orbit to the line of sight and the form of the stellar photospheric limb-darkening profile. The duration of ingress and egress also depends on the relative radii of the planet and star, and on the inclination of the orbit to the line of sight.

The two key parameters that determine the flux deficit at any given moment during the transit are the projected separation $z \equiv d/R_*$ of the centres of the planet

and the star, and the planet/star radius ratio $p \equiv R_p/R_*$. The apparent separation of the star and planet projected on the plane of the sky is $d = r \sin \alpha$, where r is the instantaneous distance of the planet from the star and α is the star–planet–observer phase angle. Calculation of the flux deficit involves integrating the surface brightness $I(\mu)$ of the photosphere over the solid angle of the part of the photosphere obscured by the planet. In the limit where the planet is much smaller than the star, a fast approximation involves using the photospheric brightness at the centre of the planet. Either approach requires a limb-darkening model, which is described by one or more auxiliary parameters u_n whose values depend on the temperature, pressure and opacity profile of the photosphere. A number of authors have published fast analytic algorithms for computing the flux deficit for a variety of limb-darkening models. The simplest of these is the very simplistic linear model

$$\frac{I(\mu)}{I_0} = 1 - u(1 - \mu), \quad (2.46)$$

where the parameters I_0 , u_n and μ are defined as in Eq. (2.6). More sophisticated treatments range from the quadratic approximation

$$\frac{I(\mu)}{I_0} = 1 - \sum_{n=1}^2 u_n(1 - \mu^n) \quad (2.47)$$

to a 4-coefficient nonlinear model which reproduces the intensity profile near the limb in a much more satisfactory manner:

$$\frac{I(\mu)}{I_0} = 1 - \sum_{n=1}^4 u_n(1 - \mu^{n/2}). \quad (2.48)$$

The most widely used formulation is that of Mandel and Agol (2002), though more recent treatments by Pál (2008) and Giménez (2006) offer improved numerical stability and precision in some circumstances. Numerous compilations of theoretical limb-darkening coefficients are available in a range of common photometric band-passes, computed from model atmospheres on grids of stellar effective temperature, surface gravity and metallicity, and fitted with the linear, quadratic and 4-coefficient nonlinear approximations. The most widely used compilations at present are those of Claret (2003, 2004) and Sing (2010).

Given a set of photometric measurements and suitable implementation of a transit model in subroutine form, the procedure for computing a single realisation of a transit model involves adopting a set of limb-darkening coefficients for the relevant passband and a value for the planet/star radius ratio p , and computing the projected separation of centres $z(t)$ at each of the times t to be considered. The output is an array of flux ratios $F(t)/F_0$ where F_0 is the stellar flux outside transit. For parameter-fitting purposes, the model is evaluated at the times of observation, though denser sampling is often used for graphical presentation of the light-curve model.

Denser time sampling is also necessary when the exposure time is long enough that the relative flux changes significantly during the exposure. This is an important issue with, for example, the long-cadence observing modes of the *CoRoT* and *Kepler* missions (Kipping 2010). Satisfactory modelling of the recorded flux in these circumstances requires integration of the instantaneous model flux, necessitating denser sampling over the exposure duration.

2.4.1 Orbital Elements

A dynamical model of the planet's orbit is needed to compute the separation of centres $z(t)$ at a sequence of times t . In addition to the scaling parameters $z_{\max} = a/R_*$ and $p = R_p/R_*$, the orbital elements of the planet must be known. For the simplest possible system comprising only a star and a planet, the epoch of periastron t_0 , orbital period P , inclination i , eccentricity e and argument of periastron ω provide a full description of the orbital motion.

As illustrated in Fig. 2.10, the true anomaly of the planet at the times of mid-transit and mid-occultation is

$$\nu_{\text{tr}} = \frac{\pi}{2} - \omega \quad \text{and} \quad \nu_{\text{occ}} = \frac{3\pi}{2} - \omega, \quad (2.49)$$

respectively.

The time delay from periastron to mid-transit for a planet in an eccentric orbit is computed from Eq. (2.49) for the true anomaly at mid-transit. Substituting ν_{tr} for ν in Eq. (2.51) yields the eccentric anomaly E_{tr} at mid-transit. The time delay is then given by

$$t_{\text{tr}} - t_0 = \frac{P}{2\pi} M_{\text{tr}} = \frac{P}{2\pi} (E_{\text{tr}} - e \sin E_{\text{tr}}). \quad (2.50)$$

A similar procedure yields the true anomaly at mid-occultation.

For the purposes of determining the scaled separation of centres z at any time, we need to calculate the mean anomaly ν as a function of time. At any time t , the true anomaly ν is computed from the mean anomaly $M = 2\pi(t - t_0)/P$ via the eccentric anomaly

$$E = 2 \tan^{-1} \left[\sqrt{\frac{1-e}{1+e}} \tan \frac{\nu}{2} \right], \quad (2.51)$$

which is related to the mean anomaly by $M = E - e \sin E$. A simple, fast iterative solution starts by estimating $E_1 = M$, then iterating

$$E_{i+1} = M + e \sin E_i. \quad (2.52)$$

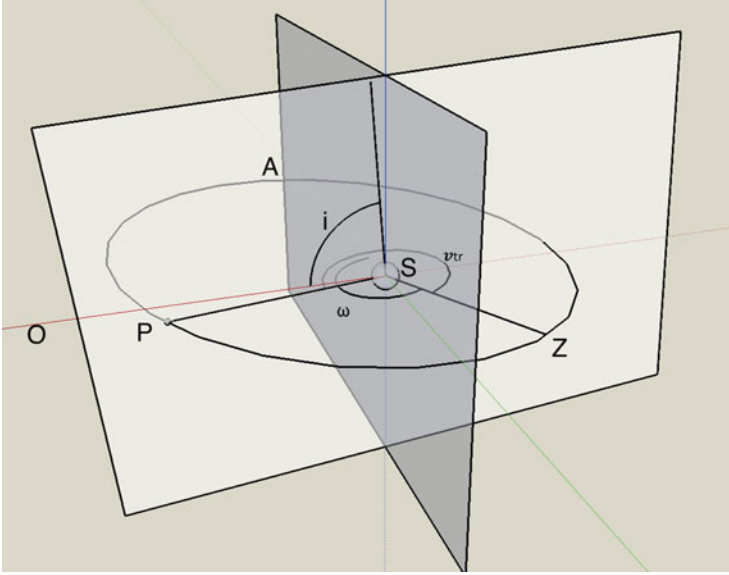


Fig. 2.10 Orbital elements of an extrasolar planet P orbiting a star S . The *red axis* points to the observer. The *green and blue axes* lie in the (*grey*) plane of the sky; the *red and blue axes*, and the orbital angular-momentum vector, lie in the *white plane*. Mid-transit occurs when the planet passes through the *white plane*. The argument of periastron ω (angle ASZ) is measured from the intersection of the planes of the orbit and the sky on the side of the orbit where the planet's motion is toward the observer O , around the star in the plane of the orbit and to the direction Z of periastron. The true anomaly ν is the angle ZSP ; here, the configuration is shown at mid-transit

On convergence,

$$\nu = 2 \tan^{-1} \left[\sqrt{\frac{1+e}{1-e}} \tan \frac{E}{2} \right]. \quad (2.53)$$

The instantaneous star–planet distance is

$$r = a(1 - e \cos E). \quad (2.54)$$

Seen from the observer's viewpoint, the planet's position along the green axis in Fig. 2.10 on the plane of the sky is

$$x_p = r \sin(\nu + \omega - \pi/2). \quad (2.55)$$

Along the projection of the orbital axis in the plane of the sky (the blue axis in Fig. 2.10),

$$z_p = -r \cos(\nu + \omega - \pi/2) \cos i. \quad (2.56)$$

The third component of the planet's cartesian position vector is toward the observer along the red axis in Fig. 2.10:

$$y_p = r \cos(v + \omega - \pi/2) \sin i. \quad (2.57)$$

The star–planet–observer phase angle, which determines the fractional illumination of the planet's visible hemisphere, is $\cos \alpha = y_p/r$. The apparent star–planet separation is thus

$$r \sin \alpha = \sqrt{x_p^2 + z_p^2}, \quad (2.58)$$

and the scaled separation is

$$z = r \sin \alpha / R_*. \quad (2.59)$$

By differentiating y_p with respect to time we obtain the planet's velocity toward the observer relative to the star:

$$\begin{aligned} v_p &= \frac{dy_p}{dv} \frac{dv}{dM} \frac{dM}{dt} \\ &= \frac{2\pi a}{P} \frac{\sin i}{\sqrt{1-e^2}} (e \cos \omega + \cos(v + \omega)). \end{aligned} \quad (2.60)$$

The component of the star's reflex motion away from the observer (along the red axis in Fig. 2.10) is then

$$v_t = K(e \cos \omega + \cos(v + \omega)) + \gamma, \quad (2.61)$$

where γ is the rate of change of distance of the system's centre of mass away from the solar-system barycentre. Note that $\sin i$ is implicit in the value of K :

$$K = \frac{2\pi a}{P} \frac{m_p}{m_* + m_p} \frac{\sin i}{\sqrt{1-e^2}}. \quad (2.62)$$

The eccentricity of the orbit modifies the durations of transits and occultations through Kepler's second law. The transverse velocity of the planet at mid-transit is obtained by differentiating Eq. (2.55) for x_p and substituting Eq. (2.49) to obtain

$$v_t = \frac{2\pi a}{P} \frac{e \sin \omega + 1}{\sqrt{1-e^2}}. \quad (2.63)$$

At first and third contact, the separation of centres is $h = 1 + R_p/R_*$. The impact parameter at mid-transit is

$$b = \frac{z_p}{R_*} = -\frac{a}{R_*} \frac{1 - e^2}{1 + e \sin \omega}. \quad (2.64)$$

For the case where $R_* \ll a$, the approximate transit duration is

$$\frac{t_{tr}}{P} \simeq \frac{R_*}{a} \frac{\sqrt{(1 + R_p/R_*)^2 - b^2}}{\pi} \frac{1 + e \sin \omega}{1 - e^2}. \quad (2.65)$$

2.4.2 Bayesian Parameter Fitting

Equations (2.59) and (2.61) provide a complete orbital model for generating synthetic fluxes and radial velocities at a set of times of observation. In the early stages of investigation immediately following detection of transits, however, radial velocities are seldom available. At this stage, we want to know if the transits are real. If they are, we also want to know the relative radii of the star and the transiting companion, and to determine whether the density of the host star is consistent with being on the main sequence.

The data comprise a sequence of observed relative fluxes or magnitudes D_i with estimated variances σ_i^2 , and a sequence of model fluxes $\mu(\boldsymbol{\theta}; t_i)$ evaluated at the times t_i of observation. The model depends on a set $\boldsymbol{\theta}$ of model parameters. Assuming the orbit to be circular and the limb-darkening coefficients to be fixed, a photometric data sequence containing multiple transits is fully described by a model with five free parameters: the epoch t_{tr} of mid-transit, the orbital period P , the scale parameters R_p/R_* and a/R_* and the impact parameter b of the orbit. If the observational errors are assumed to be independent and Gaussian, the joint probability density function (or likelihood) of obtaining the observations conditioned on the model is

$$\mathcal{L} = P(\mathbf{D}|\boldsymbol{\mu}(\boldsymbol{\theta})) = \prod_i \frac{1}{2\pi\sigma_i} \exp\left(-\frac{1}{2} \frac{(D_i - \mu(\boldsymbol{\theta}; t_i))^2}{\sigma_i^2}\right). \quad (2.66)$$

Evaluating the product and taking logs, we obtain

$$\ln \mathcal{L} = -\frac{n}{2} \ln(2\pi) - \sum_i \ln \sigma_i - \frac{1}{2} \chi^2 \quad \text{where} \quad \chi^2 = \sum_i \frac{(D_i - \mu(\boldsymbol{\theta}; t_i))^2}{\sigma_i^2}. \quad (2.67)$$

Over the last 10 years, Markov-chain Monte Carlo (MCMC) methods have become popular as a means of determining the joint posterior probability distribution of the parameter set $\boldsymbol{\theta}$ describing this problem (Holman et al. 2006; Collier

Cameron et al. 2007; Burke et al. 2007). Given a vector of state variables θ from which the model parameters can be calculated, the log likelihood is calculated. Each element θ_j of the state vector is then perturbed by a small amount, usually a Gaussian random deviate scaled to the estimated width σ_j of the posterior probability distribution for that parameter:

$$^{(k+1)}\theta_j = ^{(k)}\theta_j + \sigma_j G[0, 1]. \quad (2.68)$$

The log likelihood for this $(k + 1)$ th state vector is evaluated for the new parameter set. The decision to accept or reject the proposal is made according to the Metropolis–Hastings rule (Metropolis et al. 1953; Hastings 1970). If the log likelihood of the proposal exceeds that of its predecessor, the new state vector is accepted and written into the $(k + 1)$ th step of the chain. If, however, the log likelihood has decreased, a random number $U[0, 1]$ is drawn from the uniform distribution. If

$$\frac{^{(k+1)}\mathcal{L}}{^{(k)}\mathcal{L}} > U[0, 1], \quad (2.69)$$

then the proposal is accepted and written into the chain as before. If the proposal fails this test, the proposal is rejected and the (k) th state vector is copied into the $(k + 1)$ th step of the chain.

If the parameter uncertainties are estimated correctly and the parameters are mutually uncorrelated, the algorithm should converge quickly to a stationary state, exploring the joint posterior probability distribution of the state vector of model parameters in the vicinity of the maximum-likelihood solution. In this ideal state of affairs the proposal acceptance rate should be about 25 %, leading to a correlation length of a few steps for the chains. Unless the maximum-likelihood solution has already been found by other means, there is likely to be a “burn-in” period as the algorithm moves toward the optimal solution. Similarly, the acceptance rate may not be ideal if the jump lengths for any of the parameters are under- or over-estimated. The acceptance rate can be tuned by running the chain for a few thousand steps after achieving the stationary state, discarding the burn-in sequence and re-determining the standard deviations of the chains. The chain can then be continued with the new jump lengths, and the poorly tuned part discarded.

It is best practice to carry out formal tests such as that of Gelman and Rubin (1992) to demonstrate that the chain has reached a stationary state, and to measure and publish the correlation lengths of the chains for each of the parameters. Excessively long correlation lengths may indicate a poor choice of jump parameters, such that two or more parameters are strongly correlated with each other. When two parameters are strongly correlated, a $1\text{-}\sigma$ jump in either of them inevitably results in a strong decrease in likelihood, leading to very low acceptance rates unless the step size is reduced.

For this reason a/R_* is a poor choice as a state variable in the transit problem, as illustrated on Fig. 2.11. The orbital separation a is strongly constrained by the stellar

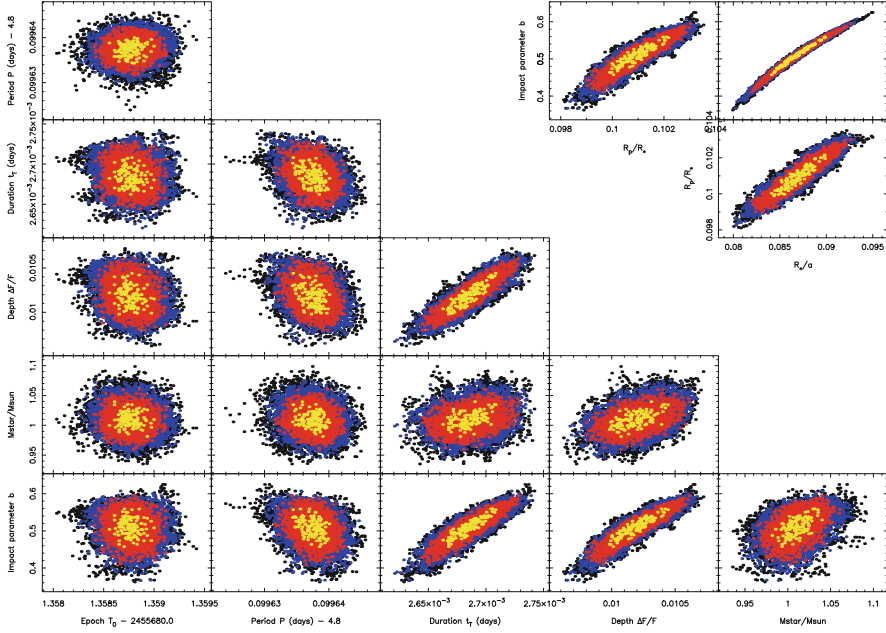


Fig. 2.11 Phase plots showing posterior probability distributions from an MCMC analysis of the transits of WASP-20b, marginalised onto all possible pairs of the six MCMC state variables T_0 , P , t_T , $\frac{\Delta F}{F}$, M_* and b . The correlations between the three physical parameters R_*/a , R_p/R_* and b governing the transit profile are also shown. The correlation between scaled stellar radius R_*/a and impact parameter b (top right) is seen to be much more extreme than that between transit duration t_T and b . Yellow, red and blue points have $2\Delta \ln \mathcal{L} > -2.30$, -6.17 and -11.8 relative to the maximum-likelihood value (Colour figure online)

mass and orbital period. The transit duration depends on both a/R_* and the impact parameter b . As b increases, R_* must also increase to preserve a good fit to the width of the transit. A better choice of state variable a/R_* is the approximation to the fractional transit duration given in Eq. (2.65), which is more nearly independent of b . The value of a/R_* is recovered trivially by inverting Eq. (2.65). Similarly, when fitting eccentric orbits, Ford (2005) recommends $e \cos \omega$ and $e \sin \omega$ in preference to e and ω . Many authors now use $\sqrt{e} \cos \omega$ and $\sqrt{e} \sin \omega$, which imposes a uniform implicit prior on the eccentricity over the range $0 < e < 1$.

Another approach, known as affine-invariant MCMC, is to determine the principal axes of the posterior probability distribution in parameter space. Jumps are then made along the principal axes, whose local directions can be determined efficiently using an ensemble of Markov chains (Goodman and Weare 2010; Gregory 2011). This method is well suited to more complex, high-dimensional problems that are

difficult to orthogonalise. A publicly available code employing this method, EMCEE, is described by Foreman-Mackey et al. (2013).¹

2.5 Candidate Validation and False-Positive Winnowing

There is an important distinction between false alarms and false positives. False alarms are objects in which transit-detection software produces a signal that passes the detection threshold, but in which no transits are in fact present. False positives, on the other hand, display genuine transit-like events caused by phenomena other than planetary transits (Fig. 2.12).

There are very strong motivations for eliminating astrophysical false positives as early as possible in the discovery process. In ground-based surveys, confirmation is almost invariably made via radial-velocity observations, and a cost of many hours of 2 m-class telescope time per target. For space-based surveys such as NASA's *Kepler* mission, there are simply too many faint candidates to be followed up spectroscopically. The influence of false positives on the statistics of planet occurrence needs to be understood.

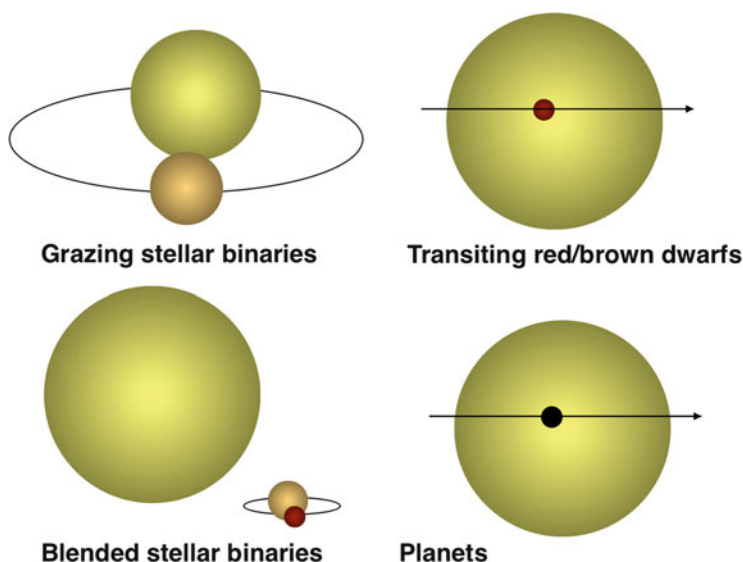


Fig. 2.12 Four types of astrophysical systems giving rise to transits or transit-like events. The blended stellar binaries may be either chance alignments or gravitationally bound hierarchical triples

¹EMCEE and many other publicly available codes may be found in the GitHub code repository at <https://github.com>.

Validation of transit candidates involves using the transit light curve itself in conjunction with existing catalogue data to determine whether the probability that the transits are caused by a planet exceeds the probability of transit-like events arising from other astrophysical causes, by a large margin.

2.5.1 *Astrophysical False Positives*

Brown (2003) identified five main classes of objects that can exhibit transit-like events in ground-based surveys. The first are the “good” ones: main-sequence stars with transiting planets, undiluted by the light of nearby objects. This leaves four classes of astrophysical false positive: undiluted main-sequence binaries that are inclined at such an angle to the line of sight that they exhibit grazing stellar eclipses, or with very low-mass stellar companions; main-sequence eclipsing binaries diluted by the light of a brighter foreground star; main-sequence binaries diluted by the light of a brighter, physically associated tertiary star and giant primary stars with main-sequence companions.

2.5.1.1 Grazing Binaries

Grazing binaries are systems in which two stars of roughly equal mass and radius are inclined at such an angle to the line of sight that they exhibit grazing stellar eclipses. This causes small, periodic dips in brightness whose depths are comparable to those expected for planets. The light curves of grazing eclipses are invariably V-shaped, lacking the quasi-flat total phase of a planetary transit. For this reason, model fits to grazing eclipses invariably yield high impact parameters. If the two components of a grazing stellar binary have different effective temperatures, the effective temperature derived for the system from colour indices in optical passbands may differ appreciably from that measured in the near infrared, e.g. using the 2MASS JHK colours. If follow-up photometry in multiple passbands is available, a colour-dependent eclipse depth is a good indicator that the cooler object is self-luminous. Finally, MCMC analysis of the light curve often yields an abnormally low stellar density for the primary, inconsistent with the mass estimated from the system colour.

2.5.1.2 Low-Mass Stellar or Substellar Companions

More plausible-looking flat-bottomed transits can occur in close stellar binaries with very unequal mass ratios. Low-mass stellar or substellar (i.e. brown dwarf) companions have radii comparable to or in some cases smaller than those of gas-giant planets. Their transits show the same rapid ingress and egress seen in planetary transits. If the companion is sufficiently self-luminous, secondary eclipses may be detectable if the discovery photometry is of sufficiently high precision. Rowe et al.

(2014) point out that it is straightforward to estimate the surface brightness of the planet’s dayside in both thermal and reflected light. A secondary eclipse whose depth exceeds the expected value indicates a self-luminous object.

A very low-mass star or brown dwarf is sufficiently massive to give significant tidal elongation of the primary star. The strong tidal interaction also leads to rapid synchronisation of the primary’s rotation, which may give rise to optical modulation by starspot activity arising from rotationally enhanced dynamo action. The ellipsoidal variation manifests itself as a sinusoidal modulation at twice the orbital frequency, with minima at the times of transit and secondary eclipse. Starspot activity also gives quasi-sinusoidal variability on the orbital frequency, often with a contribution at twice the orbital frequency. Unlike ellipsoidal variability, however, starspot modulation evolves with time. With light curves of sufficient precision (e.g. *Kepler*) relativistic Doppler beaming may also be detectable (Faigler and Mazeh 2011). If the effects of ellipsoidal variation and Doppler beaming are built into the transit model, detectable signals will yield a mass estimate for the secondary, obviating the need for radial-velocity follow-up.

2.5.1.3 Blended Eclipsing Binaries

A chance alignment of a bright, isolated star with a fainter stellar eclipsing binary produces diluted eclipses that can mimic planetary transits. In ground-based surveys, such impostors are often revealed by MCMC analysis, which yields a stellar density inconsistent with the overall colour of the system. Secondary eclipses are often present, and short-period systems may also exhibit ellipsoidal variations. Such systems may also yield inconsistent effective temperatures from optical and 2MASS colours, and exhibit wavelength-dependent eclipse depths. Space-based surveys for smaller planets are vulnerable to a related type of blend, in the form of transiting giant-planet systems diluted by a brighter, nearby star to mimic a much smaller transiting planet.

In ground-based surveys, which have notoriously poor angular resolution, such blends can be identified efficiently with follow-up photometry with larger telescopes having superior angular resolution. “On-Off” photometry, in which sequences of CCD frames are taken within and outside transit, allow faint, resolved stars showing deep eclipses on the transit ephemeris to be identified.

Batalha et al. (2010) found that many false positives caused by background eclipsing binaries display a characteristic astrometric signature in *Kepler* images. If the angular separation is non-zero, the light centroid will move toward the brighter, isolated star when the fainter binary goes into eclipse. Rowe et al. (2014) developed this method further to improve sensitivity to the very small astrometric shifts that betray this type of system. If the two stars in the faint binary have similar effective temperatures, the primary and secondary eclipses will be of comparable depth. Modelling the depths of the odd- and even-numbered transits separately is an effective way to detect primary and secondary eclipses with subtly different depths.

2.5.1.4 Hierarchical Triples

Hierarchical triples bear many similarities to blended eclipsing binaries, except that the faint eclipsing binary and the brighter diluting star are in a physically associated triple system. Their angular separations tend to be small. For example, consider a close binary with eclipses intrinsically 0.5 magnitude deep, diluted by a companion 5 magnitudes brighter at 1 AU separation. The diluted transits would appear 0.005 mag deep. At a distance of 250 pc, the angular separation would be 0.004 arcsec. During eclipse, the centroid would shift $19.5 \mu\text{as}$ toward the brighter companion. To detect such a shift would be challenging even for the ESA *Gaia* mission (de Bruijne 2012), whose single-measurement precision is of order $30 \mu\text{as}$.

2.5.2 False-Positive Winnowing

2.5.2.1 Dwarf–Giant Separation

Proper-motion measurements convey valuable information about the luminosity class of the host star, allowing Bayesian estimation of the relative likelihood that the host star is on the main sequence and not a more distant giant. Gould and Morgan (2003) found that a plot of the reduced proper motion (RPM) against $(B_T - V_T)$ colour from the TYCHO-2 catalogue was effective at separating dwarfs from giants in the planning of transit surveys. Collier Cameron et al. (2007) adapted the method to the 2MASS JHK photometric system, defining the RPM as

$$H_J = J + 5 \log(\mu) \quad (2.70)$$

and plotting it against $(J - H)$ colour. Figure 2.13 illustrates how the location of a WASP host star (in this case the slightly evolved WASP-12) in this diagram confirms its main-sequence status. The publication of the first data release from the *Gaia* mission will supersede the RPM method. With an anticipated parallax precision of $8 \mu\text{as}$ at magnitudes $V < 13$, *Gaia* will determine the distances to the existing WASP host stars, whose estimated parallaxes are all greater than $1500 \mu\text{as}$, to a precision better than 0.5 %.

2.5.2.2 Main-Sequence Prior

The stellar density derived from the transit duration provides an independent test of the host star’s main-sequence status. The relationship between stellar density and effective temperature arises from the main-sequence mass–radius relation. Tingley and Sackett (2005) pointed out that a simple power-law approximation to the mass–radius relation could be used to define a joint prior probability distribution on the mass and radius. Collier Cameron et al. (2007) describe a Bayesian approach in

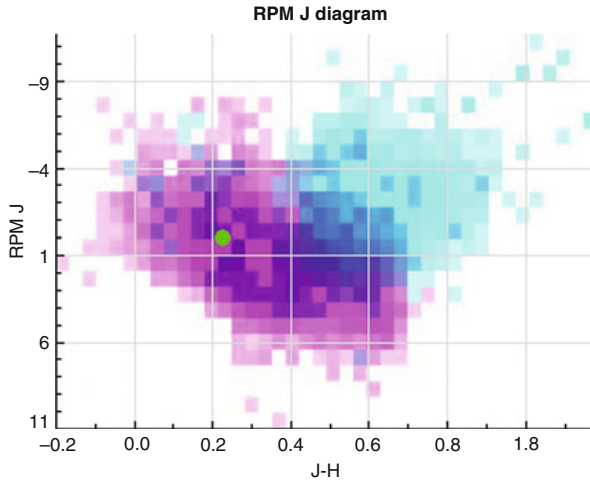


Fig. 2.13 Reduced proper-motion diagram for WASP-12 (*green point*). The magenta density plot represents the probability density for dwarfs among 2000 FGK stars for which high-resolution spectroscopic analyses have been published in the catalogues Valenti and Fischer (2005) and Cayrel de Strobel et al. (2001), cross-matched to the USNO-B1.0 catalogue for proper motions and the 2MASS catalogue for $J - H$. The *cyan plot* gives the probability density for giants from the same catalogues

which the results of MCMC analyses using priors on both mass and radius are compared with those obtained using a prior on the mass alone. The prior on the mass is obtained from the stellar effective temperature, which in turn is estimated from the $J - H$ colour. If the imposition of the main-sequence prior results in a significantly worse fit to the transit duration, the target priority is downgraded as being a likely false positive.

More recent approaches have used the stellar density derived from the transit duration directly. Sozzetti et al. (2007) pioneered the use of ρ_* as a luminosity indicator for stellar evolution models, as a means of determining the physical dimensions of the host star. The “asterodensity profiling” method of Kipping (2014) and Sliski and Kipping (2014) builds on this technique as a false-positive winnowing method.

2.5.3 Validation

Although the methods described above are suitable for selecting ground-based transit candidates for radial-velocity follow-up, the majority of *Kepler* targets are too numerous, too faint, and have expected radial-velocity amplitudes too small, for radial-velocity follow-up to be effective as a means of confirmation. In order to derive the probability density function of planets in the planet radius–orbital

separation plane, it is also necessary to understand the distributions of astrophysical false positives in the same parameter space.

The most problematic contaminants are diluted eclipsing binaries, including diluted main-sequence stars with giant planets. For an individual system, the problem can be posed in terms of fitting a candidate light curve with an eclipsing-binary model plus “third light” from an unresolved, brighter star. The parameter space for hierarchical triples is more restrictive than that for blended eclipsing binaries. Assuming the binary to be detached (as it must usually be to mimic a planetary transit without ellipsoidal variation), all three stars must lie on a single isochrone, and yield a combined colour and light curve consistent with observation.

For blended eclipsing binaries, two of the components must lie along a single isochrone. The probability of finding an eclipsing binary within a given angular separation from a brighter star must be derived from a model of the galactic stellar population in the direction of interest.

Efforts to understand the false-positive rate follow a general approach similar to the BLENDER technique developed by Torres et al. (2005, 2011). BLENDER combines follow-up spectroscopy and imaging at high angular resolution with light-curve fitting, to determine whether a given candidate is more likely to be a planetary system or a false positive. BLENDER is, however, computationally expensive, and the necessary follow-up observations are impractical for the thousands of *Kepler* candidates. This led Morton (2012) to develop an accelerated approach using a simplified light-curve fitting model in conjunction with an arbitrary combination of photometric colours, spectroscopy and adaptive-optics (AO) imaging.

The PASTIS method (Díaz et al. 2014) adopts a fully Bayesian approach to determining whether an individual transit candidate is more likely to be a planetary system or a false positive. This entails modelling the light curve and follow-up observations with a set of different scenarios (planetary system, diluted planetary system, blended or hierarchical eclipsing binary) using MCMC to determine the joint posterior probability distribution for the model parameters. It uses the marginal likelihood of each scenario to determine whether the probability of the planet hypothesis exceeds the combined probabilities of all false-positive hypotheses considered.

A by-product of this kind of validation approach is that for each object considered, it yields the relative probabilities for each of the competing hypotheses, allowing corrections to be made for the various false-positive contaminants in determining the underlying planet population (e.g. Fressin et al. 2013).

2.5.4 Multiple Transiting Systems

Among the major discoveries of the *Kepler* mission is the existence of several thousand systems in which two or more transit signatures are present. A false positive in a multiple transiting system involves either a chance alignment of a single-planet system with a blended eclipsing binary, a hierarchical triple with a

planet orbiting the bright, single component planets transiting both components of an unresolved binary star or else multiple chance alignments.

Lissauer et al. (2014) estimated the expected number of chance alignments of distant eclipsing binaries within *Kepler*'s photometric aperture. Assuming that false positives are randomly distributed among the targets, the probability of a single target displaying j false positives should be described by the Poisson distribution:

$$p(j) = \frac{\lambda^j e^{-\lambda}}{j!}, \quad (2.71)$$

for a population mean of λ false positives per target. In a sample of N targets the expected number of false positives should be $E(j) = Np(j)$. We know that the number of planet candidates per target is less than 2 %, and that the number of false positives must be even less than this, so it is reasonable to set $\lambda \ll 1$ and hence $e^{-\lambda} \approx 1$. If the probabilities that a planet displays one of more false positives, and that it hosts one or more transiting planets, are independent, the probability that a planet displays one or more false positives and hosts one or more transiting planets is simply the product of the two probabilities.

Lissauer et al. (2014) concluded that the vast majority of *Kepler* targets showing multiple transit signatures were true planetary systems. Rowe et al. (2014) used the same framework to validate a sample of 340 planetary systems comprising 851 planets with more than 99 % confidence, without having to resort to spectroscopy or high-resolution imaging for validation.

2.6 Planet Characterisation

What can we learn about the composition of an exoplanet and its atmosphere? Knowledge of the most abundant dusty and molecular constituents of protoplanetary disks and of the planets in our own solar system leads us to believe that the main refractory constituents should be iron and silicates. Water is the dominant volatile likely to be found in the solid or liquid state. Planets with sufficiently high escape velocities and low temperatures should be able to retain atmospheres of essentially primordial gaseous composition. If smaller planets retain atmospheres at all, they are likely to be of relatively high mean molecular weight.

2.6.1 Planet Radius Distribution

The first step in determining the compositions of planets is to examine the histogram of the radii of validated or confirmed planet candidates (Fig. 2.14). The abrupt drop in planet frequency above 3–4 Earth radii is thought to correspond to the threshold

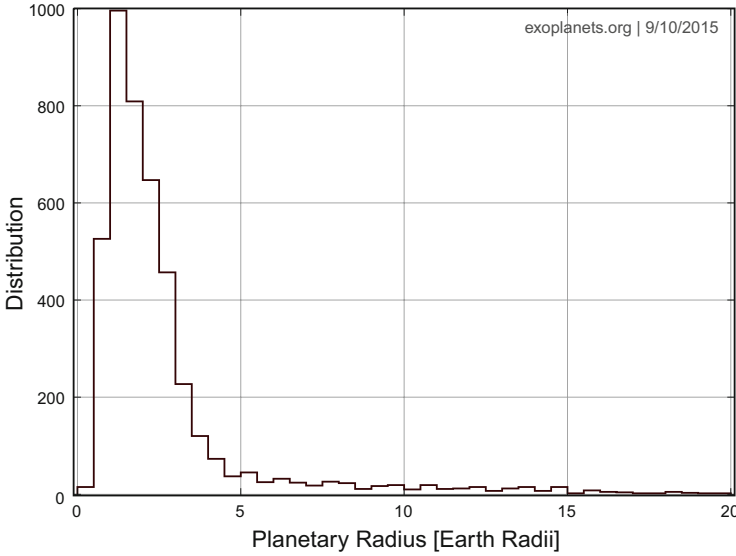


Fig. 2.14 The distribution of radii for confirmed or validated planets from the *Kepler* mission. The paucity of planets with radii less than that of the Earth reflects *Kepler*'s detection threshold rather than any feature of the underlying planet population

mass above which runaway gas accretion occurs, leading to the formation of gas-giant planets (Marcy et al. 2014).

2.6.2 Mass–Radius Relation and Planetary Composition

When the reflex orbital motion of the host star is measurable, and a reliable estimate of the stellar radius is available, the planetary density (and hence mass) can be determined directly using Eq. (2.15) or (2.16). At masses below that of Saturn, planetary radii generally decrease with increasing mass, but the factor-of-two spread in radii at a given mass implies a wide range of compositions (Fig. 2.15). At first glance the radius of a planet alone does not appear to be a reliable indicator of its composition. The radius does, however, appear to give useful insight into the presence or absence of a gaseous envelope. Lopez and Fortney (2014) computed a series of models with a varied mix of iron/silicate and water in the planetary interior, with overlying envelopes of H and He. They found that planets smaller than 1.6 Earth radii cannot retain significant envelopes of H and He, irrespective of interior composition. Planetary radii increase steeply for 1.6–10 Earth radii as the envelope fraction by mass increases from zero to 100 %.

The mass–radius relation for giant planets discovered in ground-based transit surveys (Fig. 2.5) reveals the existence of a large number of inflated hot Jupiters,

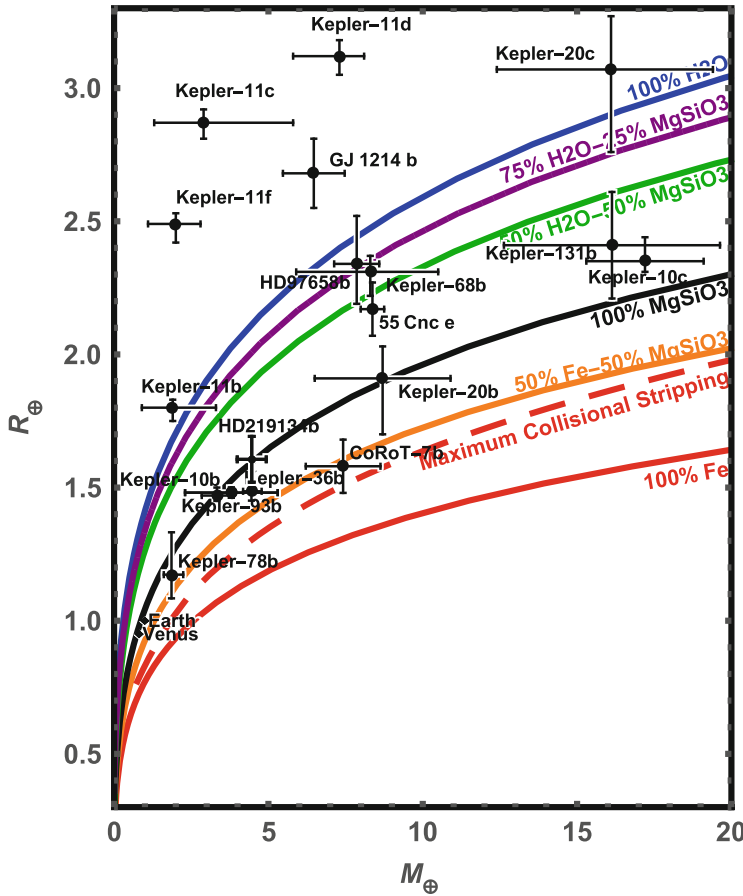


Fig. 2.15 The mass-radius relation for transiting super-Earths and mini-Neptunes whose masses have been determined either by radial-velocity follow-up or by modelling their transit-timing variations. The compositional contours are based on the work of Zeng and Sasselov (2013, 2014). HD 219134b was added with the online tool at https://www.cfa.harvard.edu/~lzeng/Exoplanet_Models.html

whose radii are greatly in excess of the values predicted by isolated models. A variety of hypotheses have been advanced for the source of internal energy needed to support such inflated radii, ranging from tidal heating during orbit circularisation (Bodenheimer et al. 2001, 2003; Jackson et al. 2008), to ohmic dissipation in partially ionised winds blowing across the planetary magnetic field (Batygin and Stevenson 2010; Batygin et al. 2011; Laughlin et al. 2011) and to irradiation by the host star (Guillot 2005). At present, irradiation appears to be the most compelling explanation. Enoch et al. (2012) found a strong correlation between planet radius and planetary equilibrium temperature for Jupiter-mass planets. Ohmic

dissipation may, however, be important as a means of converting irradiating flux in the atmosphere to internal energy in the deep interior.

2.6.3 Dayside Irradiation and Weather Patterns

The equilibrium temperature of a planet orbiting at distance a from a host star of radius R_* and effective temperature T_* may be estimated by balancing power received against power re-radiated, approximating the planet as a black body radiator:

$$\frac{4\pi R_p^2}{f} \sigma T_{\text{eq}}^4 = \frac{4\pi R_*^2 \sigma T_*^4}{4\pi a^2} \pi R_p^2 (1 - A). \quad (2.72)$$

This expression makes simple corrections for the Bond albedo A and a factor $1 < f < 2$ representing the efficiency of heat transport from the dayside to the nightside of a tidally locked planet. Isotropic re-radiation is represented by $f = 1$, while re-radiation from the dayside only requires $f = 2$.

In the *Kepler* bandpass, out-of-transit variations are seen in a number of the brighter hot Jupiters, notably HAT-P-7b (Borucki et al. 2009), TrES-2b (Kipping and Bakos 2011) and Kepler-7b (Demory et al. 2011). Being modulated on the planetary orbital period rather than the stellar rotation period, they are attributable to the planetary phase curve rather than stellar activity. At these short wavelengths the phase curve arises mainly from starlight reflected from the planetary dayside, though in very close-orbiting planets far-red thermal emission may be seen as an elevation in the flux at the shoulders of primary transit relative to the purely stellar flux seen at secondary occultation (Hu et al. 2015, and Fig. 2.2).

The temperature contrast between the dayside and the nightside of a planet can be determined directly by observing the full phase curve of the planet around the orbit at thermal-infrared wavelengths. Knutson et al. (2007) made the first phase curve observation of HD 189733b at a wavelength of $8\text{ }\mu\text{m}$, covering both the primary transit and the secondary eclipse. The difference in planetary flux between the dayside and nightside hemispheres is measured as shown schematically in Fig. 2.2, and yields brightness temperatures of $1212 \pm 11\text{ K}$ and $973 \pm 33\text{ K}$, respectively. The phase curve is asymmetric, with minimum brightness occurring slightly after transit and maximum brightness slightly before secondary occultation.

Similar displacements of the hottest part of the dayside from the substellar point have since been observed to varying degrees in the phase curves of WASP-18b (Maxted et al. 2013), HAT-P-2b (Lewis et al. 2013) and WASP-14b (Wong et al. 2015). Theoretical studies of heat transport between the daysides and the nightsides of these planets (Showman et al. 2009; Dobbs-Dixon and Agol 2013) have adapted global atmospheric circulation models to study the consequences of extreme irradiation of the daysides of these tidally locked planets. The simulations

typically produce a super-rotating equatorial jet and large temperature differences between the dayside and nightside.

2.6.4 *Transit Spectroscopy*

In planets with extended atmospheres, the transit depth is wavelength-dependent. The size of the planet's silhouette is determined by the height at which light passing through the atmosphere at grazing incidence encounters an optical depth of order unity. Brown (2001) developed a simple model for predicting the variation of transit depth with wavelength for atmospheres containing common molecular absorbers such as CO, water and methane. The strength of these absorption features depends on the presence or absence of an opaque cloud deck, and its height in the atmosphere. A high cloud deck produces a nearly featureless spectrum, whereas a clear atmosphere shows molecular absorption or emission, depending on the form of the temperature–pressure structure in the upper atmosphere.

The first successful detection of spectral absorption in a planetary atmosphere was made by Charbonneau et al. (2002), who used time-resolved spectroscopy with the STIS instrument aboard HST to detect the enhancement in the transit depth at the wavelength of the NaI D lines. This suggested that even if a cloud deck was present, atomic sodium was sufficiently abundant in the overlying atmosphere to give a measurable increase in transit depth at the wavelengths of the sodium lines.

Pont et al. (2013) measured the transit depth for HD189733b in several band-passes ranging from the UV to the near infrared, using the STIS, ACS and WFC3 instruments aboard the Hubble Space Telescope. They found an essentially featureless transmission spectrum longward of 1 μm . Shortward of this, the transit depth increased monotonically toward shorter wavelengths from the optical to the near UV. They attributed the featureless infrared spectrum and short-wavelength rise to Rayleigh scattering, presenting grazing-incidence optical depths greater than unity at progressively greater heights above a dusty cloud deck. Pont et al. (2013) pointed out that great care needs to be taken with this type of observation if the host star is magnetically active. Unocculted starspots on the visible stellar hemisphere also deepen the transit by an amount that depends on the spot/photosphere contrast, which increases toward shorter wavelengths. Nonetheless, the Rayleigh scattering slope holds great promise as a means for determining planetary surface gravities (de Wit and Seager 2013), particularly for planets of unspotted early type stars, whose rapid rotation makes it difficult or impossible to measure the reflex orbital motion of the host star.

2.6.5 Time-Resolved High-Resolution Spectroscopy

As it transits the face of its host star, a planet in a near-circular orbit exhibits a high radial acceleration. Given Eq. (2.14) for the radial acceleration of the star, the radial acceleration of the planet itself is

$$\dot{v}_r \simeq \frac{GM_*}{a^2} = \frac{2\pi K}{P} \frac{M_*}{M_p}. \quad (2.73)$$

Using Eq. (2.8) for the approximate transit duration in terms of R_*/a and Eq. (2.73), the range of velocities swept out by the planet during the transit is

$$\delta v_r \simeq \frac{P}{\pi} \frac{R_*}{a} \frac{2\pi K}{P} \frac{M_*}{M_p}. \quad (2.74)$$

If narrow spectral features originating in the planet's atmosphere can be detected and tracked through transit at high spectral resolution, δv_r becomes directly observable, giving direct and model-independent access to the planet/star mass ratio.

Snellen et al. (2010) used time-resolved spectroscopy during a transit of HD209458b with the CRILES near-IR echelle spectrograph at the VLT to achieve the first successful observation of this kind. They assumed that CO would be present in the planet's atmosphere, and that the transit depth would therefore increase slightly at the wavelengths of CO absorption features. After careful correction for telluric absorption, and subtraction of the mean stellar spectrum, they cross-correlated the residuals with a model spectrum of CO. The expected feature was weakly detected in the cross-correlation functions of the individual spectra. The radial acceleration of the CCF peak yielded a mass estimate $M_* = 1.00 \pm 0.22 M_\odot$ for the host star. In addition, the peak showed a constant velocity offset of 2 km s^{-1} with respect to the system centre of mass, suggesting the presence of supersonic winds blowing toward the planetary nightside.

In addition to revealing the mass of the host star, this technique allows individual molecular species to be identified unambiguously from their unique absorption-line patterns. Moreover, a variant of this method has been applied successfully to the molecular signatures of CO and/or water in the dayside thermal spectra of the non-transiting planets τ Boo b, 51 Peg b and HD 170049b (Brogi et al. 2012, 2013, 2014), as well as the transiting planet HD 189733b (Birkby et al. 2013).

2.7 The Future

Planets that transit their host stars are readily detected in surveys of large numbers of stars. Transiting systems brighter than about 12th magnitude are particularly valuable, because radial-velocity observations allow the planetary mass and bulk density to be determined with 4 m-class telescopes.

New wide-field surveys are currently either in progress or in preparation, whose goal is to increase the number of bright stars hosting small planets, enabling reliable mass determination. NGTS (Sect. 2.2.1) and the NASA *TESS* mission (Ricker et al. 2015) (whose launch is anticipated in 2018) aim to detect large numbers of planets in the 1–4 Earth-radius range orbiting bright K and early M stars. The small radii of the host stars yield comparatively deep transits for small planets, enabling future atmospheric characterisation with larger instruments.

Most valuable of all, however, are the handful of transiting systems bright enough for atmospheric characterisation using either transmission spectroscopy during transit or spectral subtraction at secondary eclipse. The very brightest among these are objects like the super-Earth HD 219134b (Motalebi et al. 2015), and the hot Jupiters HD 209458b and HD 189733b. All of these were discovered in radial-velocity surveys, with the transits subsequently being detected with dedicated space-based or ground-based follow-up photometry. One of the key goals of the Swiss-led ESA S-class mission *CHEOPS* (Broeg et al. 2014), also due for launch in 2018, will be to carry out this type of follow-up on bright stars with low-mass planets, in order to provide targets for subsequent atmospheric characterisation with future large facilities such as *JWST* and the new generation of 20–40 m-class ground-based telescopes.

Although *TESS* will cover the whole sky during its 2-year baseline mission, the stare time on each field of view will be restricted to a month or so. While this allows exploration of the region around M dwarfs where planetary equilibrium temperatures might allow liquid water to exist, the search for “Earth twins” orbiting solar-type stars must await the launch of the ESA M3 mission *PLATO2.0* (Rauer et al. 2014) in 2024 or so. *PLATO2.0*’s 34 small-aperture telescopes will conduct two long pointed campaigns over a field of view 20 times greater than that of *Kepler*, giving access to a much brighter population. Asteroseismology of the host stars of transiting planets will yield precise stellar parameters and ages, opening up the possibility of studying the evolution of planetary atmospheres over the nuclear-burning lifetimes of solar-type stars.

Acknowledgements Andrew Collier Cameron acknowledges the support of the meeting organisers for travel and accommodation at the meeting, and thanks Dr. Raphaëlle Haywood for insightful proof-reading and scientific input.

References

- Aigrain, S., Hodgkin, S.T., Irwin, M.J., Lewis J.R., Roberts S.J.: Mon. Not. R. Astron. Soc. **447**, 2880 (2015)
- Alonso, R., et al.: Astrophys. J. **613**, L153 (2004)
- Alsubai, K.A., et al.: Anal. Chim. Acta **63**, 465 (2013)
- Auvergne, M., et al.: Astron. Astrophys. **506**, 411 (2009)
- Bakos, G., Noyes, R.W., Kovács, G., Stanek, K.Z., Sasselov, D.D., Domsa, I.: Publ. Astron. Soc. Pac. **116**, 266 (2004)

- Bakos, G.Á., et al.: *Astrophys. J.* **710**, 1724 (2010)
- Bakos, G.Á., et al.: *Publ. Astron. Soc. Pac.* **125**, 154 (2013)
- Batalha, N.M., et al.: *Astrophys. J.* **713**, L103 (2010)
- Batygin, K., Stevenson, D.J.: *Astrophys. J.* **714**, L238 (2010)
- Batygin, K., Stevenson, D.J., Bodenheimer, P.H.: *Astrophys. J.* **738**, 1 (2011)
- Birkby, J.L., de Kok, R.J., Brogi, M., de Mooij, E.J.W., Schwarz, H., Albrecht, S., Snellen, I.A.G.: *Mon. Not. R. Astron. Soc.* **436**, L35 (2013)
- Bodenheimer, P., Lin, D.N.C., Mardling, R.A.: *Astrophys. J.* **548**, 466 (2001)
- Bodenheimer, P., Laughlin, G., Lin, D.N.C.: *Astrophys. J.* **592**, 555 (2003)
- Borucki, W.J., et al.: *Science* **325**, 709 (2009)
- Borucki, W.J., et al.: *Science* **327**, 977 (2010)
- Bouchy, F., Pont, F., Santos, N.C., Melo, C., Mayor, M., Queloz, D., Udry, S.: *Astron. Astrophys.* **421**, L13 (2004)
- Bouchy, F., Pont, F., Melo, C., Santos, N.C., Mayor, M., Queloz, D., Udry, S.: *Astron. Astrophys.* **431**, 1105 (2005)
- Broeg, C., Benz, W., Thomas, N.: *CHEOPS* team. *Contrib. Astron. Observ. Skalnaté Pleso* **43**, 498 (2014)
- Brogi, M., Snellen, I.A.G., de Kok, R.J., Albrecht, S., Birkby, J., de Mooij, E.J.W.: *Nature* **486**, 502 (2012)
- Brogi, M., Snellen, I.A.G., de Kok, R.J., Albrecht, S., Birkby, J.L., de Mooij, E.J.W.: *Astrophys. J.* **767**, 27 (2013)
- Brogi, M., de Kok, R.J., Birkby, J.L., Schwarz, H., Snellen, I.A.G.: *Astron. Astrophys.* **565**, A124 (2014)
- Brown, T.M.: *Astrophys. J.* **553**, 1006 (2001)
- Brown, T.M.: *Astrophys. J.* **593**, L125 (2003)
- Burke, C.J., et al.: *Astrophys. J.* **671**, 2115 (2007)
- Carter, J.A., Winn, J.N.: *Astrophys. J.* **704**, 51 (2009)
- Cayrel de Strobel, G., Soubiran, C., Ralite, N.: *Astron. Astrophys.* **373**, 159 (2001)
- Charbonneau, D., Brown, T.M., Latham, D.W., Mayor, M.: *Astrophys. J.* **529**, L45 (2000)
- Charbonneau, D., Brown, T.M., Noyes, R.W., Gilliland, R.L.: *Astrophys. J.* **568**, 377 (2002)
- Claret, A.: *Astron. Astrophys.* **401**, 657 (2003)
- Claret, A.: *Astron. Astrophys.* **428**, 1001 (2004)
- Collier Cameron, A., et al.: *Mon. Not. R. Astron. Soc.* **373**, 799 (2006)
- Collier Cameron, A., et al.: *Mon. Not. R. Astron. Soc.* **380**, 1230 (2007)
- de Bruijne, J.H.J.: *Astrophys. Space Sci.* **341**, 31 (2012)
- de Wit, J., Seager, S.: *Science* **342**, 1473 (2013)
- Demory, B.-O., et al.: *Astrophys. J.* **735**, L12 (2011)
- Díaz, R.F., Almenara, J.M., Santerne, A., Moutou, C., Lethuillier, A., Deleuil, M.: *Mon. Not. R. Astron. Soc.* **441**, 983 (2014)
- Dobbs-Dixon, I., Agol, E.: *Mon. Not. R. Astron. Soc.* **435**, 3159 (2013)
- Enoch, B., Collier Cameron, A., Horne, K.: *Astron. Astrophys.* **540**, A99 (2012)
- Faigler, S., Mazeh, T.: *Mon. Not. R. Astron. Soc.* **415**, 3921 (2011)
- Ford, E.B.: *Astron. J.* **129**, 1706 (2005)
- Foreman-Mackey, D., Hogg, D.W., Lang, D., Goodman, J.: *Publ. Astron. Soc. Pac.* **125**, 306 (2013)
- Fressin, F., et al.: *Astrophys. J.* **766**, 81 (2013)
- Gardner, J.P., et al.: *Space Sci. Rev.* **123**, 485 (2006)
- Gelman, A., Rubin, D.B.: *Stat. Sci.* **7**, 457 (1992)
- Gibson, N.P.: *Mon. Not. R. Astron. Soc.* **445**, 3401 (2014)
- Giménez, A.: *Astron. Astrophys.* **450**, 1231 (2006)
- Goodman, J., Weare, J.: *Commun. Appl. Math. Comput. Sci.* **5**, 65 (2010)
- Gould, A., Morgan, C.W.: *Astrophys. J.* **585**, 1056 (2003)
- Gregory, P.C.: *Mon. Not. R. Astron. Soc.* **410**, 94 (2011)
- Guillot, T.: *Annu. Rev. Earth Planet. Sci.* **33**, 493 (2005)
- Hastings, W.K.: *Biometrika* **57**, 97 (1970)

- Haywood, R.D., et al.: (2014) *Mon. Not. R. Astron. Soc.* **443**, 2517
- Henry, G.W., Marcy, G.W., Butler, R.P., Vogt, S.S.: *Astrophys. J.* **529**, L41 (2000)
- Høg, E., et al.: *Astron. Astrophys.* **355**, L27 (2000)
- Holman, M.J., et al.: *Astrophys. J.* **652**, 1715 (2006)
- Howell, S.B., et al.: (2014) *Publ. Astron. Soc. Pac.* **126**, 398
- Hu, R., Demory, B.-O., Seager, S., Lewis, N., Showman, A.P.: *Astrophys. J.* **802**, 51 (2015)
- Jackson, B., Greenberg, R., Barnes, R.: *Astrophys. J.* **681**, 1631 (2008)
- Kipping, D.M.: *Mon. Not. R. Astron. Soc.* **408**, 1758 (2010)
- Kipping, D.M.: *Mon. Not. R. Astron. Soc.* **440**, 2164 (2014)
- Kipping, D., Bakos, G.: *Astrophys. J.* **733**, 36 (2011)
- Knutson, H.A., et al.: *Nature* **447**, 183 (2007)
- Kovács, G., Zucker, S., Mazeh, T.: *Astron. Astrophys.* **391**, 369 (2002)
- Kovács, G., Bakos, G., Noyes, R.W.: *Mon. Not. R. Astron. Soc.* **356**, 557 (2005)
- Laughlin, G., Crismani, M., Adams, F.C.: *Astrophys. J.* **729**, L7 (2011)
- Lewis, N.K., et al.: *Astrophys. J.* **766**, 95 (2013)
- Lissauer, J.J., et al.: *Astrophys. J.* **784**, 44 (2014)
- Lopez, E.D., Fortney, J.J.: *Astrophys. J.* **792**, 1 (2014)
- Mandel, K., Agol, E.: *Astrophys. J.* **580**, L171 (2002)
- Marcy, G., Butler, R.P., Fischer, D., Vogt, S., Wright, J.T., Tinney, C.G., Jones, H.R.A.: *Prog. Theor. Phys. Suppl.* **158**, 24 (2005)
- Marcy G.W., et al.: *Astrophys. J. Suppl. Ser.* **210**, 20 (2014)
- Maxed, P.F.L., et al.: *Mon. Not. R. Astron. Soc.* **428**, 2645 (2013)
- Mayor, M., Queloz, D.: *Nature* **378**, 355 (1995)
- McCullough, P.R., Stys, J.E., Valenti, J.A., Fleming, S.W., Janes, K.A., Heasley, J.N.: *Publ. Astron. Soc. Pac.* **117**, 783 (2005)
- Metropolis, N., Rosenbluth, A.W., Rosenbluth, M.N., Teller, A.H., Teller, E.: *J. Chem. Phys.* **21**, 1087 (1953)
- Morton, T.D.: *Astrophys. J.* **761**, 6 (2012)
- Motalebi, F., et al.: (2015) arXiv:1507.08532
- Pál, A.: *Mon. Not. R. Astron. Soc.* **390**, 281 (2008)
- Pepper, J., et al.: *Publ. Astron. Soc. Pac.* **119**, 923 (2007)
- Pollacco, D.L., et al.: *Publ. Astron. Soc. Pac.* **118**, 1407 (2006)
- Pont, F., Zucker, S., Queloz, D.: *Mon. Not. R. Astron. Soc.* **373**, 231 (2006)
- Pont, F., Sing, D.K., Gibson, N.P., Aigrain, S., Henry, G., Husnoo, N.: *Mon. Not. R. Astron. Soc.* **432**, 2917 (2013)
- Queloz, D., et al.: *Astron. Astrophys.* **506**, 303 (2009)
- Rauer, H., et al.: *Exp. Astron.* **38**, 249 (2014)
- Ricker, G.R., et al.: *J. Astron. Telesc. Instrum. Syst.* **1**, 014003 (2015)
- Rowe, J.F., et al.: *Astrophys. J.* **784**, 45 (2014)
- Seager, S., Mallén-Ornelas, G.: *Astrophys. J.* **585**, 1038 (2003)
- Showman, A.P., Fortney, J.J., Lian Y., Marley, M.S., Freedman, R.S., Knutson, H.A., Charbonneau, D.: *Astrophys. J.* **699**, 564 (2009)
- Sing, D.K.: *Astron. Astrophys.* **510**, A21 (2010)
- Sliski, D.H., Kipping, D.M.: *Astrophys. J.* **788**, 148 (2014)
- Smith, J.C., et al.: *Publ. Astron. Soc. Pac.* **124**, 1000 (2012)
- Snellen, I.A.G., de Kok, R.J., de Mooij, E.J.W., Albrecht, S.: *Nature* **465**, 1049 (2010)
- Sozzetti, A., Torres, G., Charbonneau, D., Latham, D.W., Holman, M.J., Winn, J.N., Laird, J.B., O'Donovan, F.T.: *Astrophys. J.* **664**, 1190 (2007)
- Southworth, J., Wheatley, P.J., Sams, G.: *Mon. Not. R. Astron. Soc.* **379**, L11 (2007)
- Struve, O.: *Org. Biomol. Chem.* **72**, 199 (1952)
- Tamuz, O., Mazeh, T., Zucker, S.: *Mon. Not. R. Astron. Soc.* **356**, 1466 (2005)
- Tingley, B., Sackett, P.D.: *Astrophys. J.* **627**, 1011 (2005)
- Torres, G., Konacki, M., Sasselov, D.D., Jha S.: *Astrophys. J.* **619**, 558 (2005)
- Torres, G., et al.: *Astrophys. J.* **727**, 24 (2011)

- Udalski, A., Szymanski, M., Kaluzny, J., Kubiak, M., Mateo, M.: *Anal. Chim. Acta* **42**, 253 (1992)
- Udalski, A., et al.: *Anal. Chim. Acta* **52**, 1 (2002a)
- Udalski, A., Zebrun, K., Szymanski, M., Kubiak, M., Soszynski, I., Szewczyk, O., Wyrzykowski, L., Pietrzynski, G.: *Anal. Chim. Acta* **52**, 115 (2002b)
- Udalski, A., Szewczyk, O., Zebrun, K., Pietrzynski, G., Szymanski, M., Kubiak, M., Soszynski, I., Wyrzykowski, L.: *Anal. Chim. Acta* **52**, 317 (2002c)
- Valenti, J.A., Fischer, D.A.: *Astrophys. J. Suppl. Ser.* **159**, 141 (2005)
- Wheatley, P.J., et al.: Exploring the formation and evolution of planetary systems. *Proc. Int. Astron. Union Symp.* **299**, 311–312 (2014)
- Wong, I., et al.: *Astrophys. J.* **811**, 122 (2015)
- Zeng, L., Sasselov, D.: *Publ. Astron. Soc. Pac.* **125**, 227 (2013)
- Zeng, L., Sasselov, D.: *Astrophys. J.* **784**, 96 (2014)

Methods of Detecting Exoplanets

1st Advanced School on Exoplanetary Science

Bozza, V.; Mancini, L.; Sozzetti, A. (Eds.)

2016, XV, 252 p. 109 illus., 35 illus. in color., Hardcover

ISBN: 978-3-319-27456-0